Particle-in-Cell Code BEAMPATH for Beam Dynamics Simulations in Linear Accelerators and Beamlines*

Yuri K. Batygin

Stanford Linear Accelerator Center, Stanford University, Stanford, CA 94309

Abstract

A code library BEAMPATH for 2 - dimensional and 3 - dimensional space charge dominated beam dynamics study in linear particle accelerators and beam transport lines is developed. The program is used for particle-in-cell simulation of axial-symmetric, quadrupole-symmetric and z-uniform beams in a channel containing RF gaps, radio-frequency quadrupoles, multipole lenses, solenoids and bending magnets. The programming method includes hierarchical program design using program-independent modules and a flexible combination of modules to provide the most effective version of the structure for every specific case of simulation. Numerical techniques as well as the results of beam dynamics studies are presented.

1 INTRODUCTION

The design of particle accelerators with high brightness beams requires careful control of particle dynamics with space charge forces of the beam. The particle-in-cell (PIC) method is a well established technique for space charge dominated beam study. Numerous codes cover a wide range of problems connected with the simulation of beam transport and acceleration in linacs and circular accelerators using 2- and 3- dimensional approach. Among others the well-developed codes are PARMILA [1], PARMTEQ [2], WARP3D [3], SIMPSONS [4], ACCSIM [5], SAMBA [6], ORBIT [7], TRACK3D [8], TOPKARK [9]. In spite of the many years of experience in high-current beam dynamics simulation, the number of problems to be solved and their complexity are increasing. The BEAMPATH code has been developing since the beginning of 1980's as a many-purpose tool for studying beam dynamics with space charge in linear accelerators and beamlines [10]. The scope of the program includes beam transport in a channel with arbitrary order multipoles, solenoids and bending magnets, beam acceleration with space charge in radio-frequency (RF) cavities, waveguides and radio-frequency quadrupole (RFQ) structures (see Table 1). The aim of the project was to create a flexible software, which could be adjusted for frequently changeable problems. As a result, this single code covers many issues, typically distributed among different codes:

- 2D and 3D space charge effects for different beam geometry,
- spin depolarization effects,
- beam loading in accelerating waveguides,
- particle tracking in commonly used beamline elements and accelerating structures,
- symplectic integration of particle trajectories,
- generation of typical beam distributions as well as dealing with user specified distribution.

In this paper a detailed description of numerical algorithms as well as data on accuracy and efficiency of the program are presented.

2 SELF-CONSISTENT PROBLEM FOR NUMERICAL BEAM DYNAMICS STUDY WITH SPACE CHARGE

Consider the propagation of an intense charged particle beam in an accelerating-focusing channel. For the beam dynamics study, the particle-in-cell method is used [11]. The beam is represented as a combination of a large number, $N \gg 1$, of modeling particles (macropaticles) with the same charge-to-mass ratio, q/m, as in the real beam.

The transported beam is substituted by a combination of charged lines (strings). The bunched beam consists of charged clouds. The dynamics of particles in the RF field is simulated inside a quasi-period of the structure with the length of $\Lambda = \frac{\bar{v}}{c}\lambda$, where $\bar{v} = \bar{\beta}c$ is the average longitudinal velocity of the accelerated particles, c is the velocity of light, $\lambda = 2\pi c/\omega$ is the wavelength and ω is

the circular frequency. The quasi-period moves in the longitudinal direction with the velocity $\bar{v}$. The quasi-period is limited transversely by an aperture of the structure. The simulation is performed in 6-dimensional phase space of particle positions x, y, z, and mechanical momenta p_x, p_y, p_z.

At the initial moment of time, phase-space is filled with macroparticles using a random number generator (see Section 5). Particle trajectories are integrated in the field which is a combination of external field and self space-charge field of the beam. During simulations the macroparticle is stopped if it touches an aperture boundary (transverse loss). If the particle leaves the quasi-period in the longitudinal direction (longitudinal loss), its trajectory is integrated, but the Coulomb influence on the other particles is neglected.

The single-particle Hamiltonian in curvilinear coordinates x, y, z (see Fig. 1) is given by:

$$H = c \sqrt{ m^2c^2 + (\frac{P_z}{1 + \frac{x}{R(z)}} - qA_z)^2 + (P_x - qA_x)^2 + (P_y - qA_y)^2 } + qV , \qquad (2.1)$$

where P_x, P_y, P_z are components of the canonical-conjugate momentum of the particle, A_x, A_y, A_z are components of the vector-potential, V is a scalar potential of the structure and R(z) is a the radius of curvature of a reference trajectory. The Hamiltonian equations of motion are

$$\frac{dx}{dt} = \frac{\partial H}{\partial P_x}, \qquad \frac{dy}{dt} = \frac{\partial H}{\partial P_y}, \qquad \frac{dz}{dt} = \frac{\partial H}{\partial P_z} , \qquad (2.2)$$

$$\frac{dP_x}{dt} = - \frac{\partial H}{\partial x} , \qquad \frac{dP_y}{dt} = - \frac{\partial H}{\partial y} , \qquad \frac{dP_z}{dt} = - \frac{\partial H}{\partial z} . \qquad (2.3)$$

Instead of vector potential $\vec{A}$ and scalar potential V it is more convenient to use an electric field $\vec{E} = - q\, \partial\vec{A}/\partial t$ - grad V and a magnetic field $\vec{B} = rot\, \vec{A}$. The transformation from canonical momentum $\vec{P}$ to mechanical momentum $\vec{p} = \vec{P} - q\vec{A}$ gives a set of equations of motion:

$$\frac{dx}{dt} = \frac{p_x}{m\,\gamma},$$

$$\frac{dy}{dt} = \frac{p_y}{m\,\gamma} , \qquad\qquad \gamma = \sqrt{1 + \frac{p_x^2 + p_y^2 + p_z^2}{m^2\, c^2}} ,$$

$$\frac{dz}{dt} = \frac{p_z}{m\,\gamma\,(1 + \frac{x}{R})} ,$$

$$\qquad\qquad\qquad\qquad\qquad\qquad (2.4)$$

$$\frac{dp_x}{dt} = \frac{p_z^2}{m\gamma\,(R + x)} + qE_x + \frac{q}{m\gamma}\,(p_y\, B_z - p_z\, B_y),$$

$$\frac{dp_y}{dt} = qE_y + \frac{q}{m\gamma}\,(p_z\, B_x - p_x\, B_z),$$

$$\frac{dp_z}{dt} = - \frac{p_z\, p_x}{m\gamma\,(R + x)} + qE_z + \frac{q}{m\gamma}\,(p_x\, B_y - p_y\, B_x).$$

Integration is performed with a fixed time step, δt, utilizing the integrator of Section 3. Time t is selected as an independent variable rather than a longitudinal coordinate, z, because in the latest case the right - hand sides of equations of motion have to be divided by the square of the velocity, v_z^2. Because the particle velocity, $v_z = p_z/\gamma$, is a dependent variable and is defined with some error, the integration of the equations of motion in this case is less accurate.

Electrical and magnetic fields acting on the particle are a combination of external fields, $\vec{E}_{ext}$, $\vec{B}_{ext}$, and space charge fields of the beam, $\vec{E}_{sc}$, $\vec{B}_{sc}$ (see Fig. 2):

$$\vec{E} = \vec{E}_{ext} + \vec{E}_{sc}, \tag{2.5}$$

$$\vec{B} = \vec{B}_{ext} + \vec{B}_{sc}. \tag{2.6}$$

The external fields are given functions of coordinates and time (see Section 6). The space charge field of the beam is renewed at every elementary integration step via solution of the Poisson's equation in the moving frame (see Section 7). This approach provides self-consistent treatment of the problem, because particles move in the field, which depends on particle dynamics. In subsequent Sections the numerical algorithms and results of numerical simulations will be discussed.

3 NUMERICAL INTEGRATION OF RELATIVISTIC PARTICLE TRAJECTORIES IN CURVILINEAR COORDINATES

The numerical integrator of particle trajectories in PIC models has to keep as many properties of the original physical system, as possible, and, to be effective, stable and accurate [11]. The main properties of a Hamiltonian system are symplecticity (preservation of phase space volume) and conservation of energy (for systems with time-independent Hamiltonian). The numerical solution depends on the arbitrary value of the integration step and is not equivalent to the exact solution of differential equations of motion. The integrator cannot keep all the properties of the original physical system [12]. In the BEAMPATH code the well-known integration scheme [11] with modifications for a curvilinear system of coordinates is used.

3.1. Integrator of particle trajectories

Let us introduce dimensionless variables:

$$\tau = \frac{\delta t \cdot c}{\lambda}, \quad R \to \frac{R}{\lambda}, \quad x \to \frac{x}{\lambda}, \quad p_x \to \frac{p_x}{m\,c}, \quad E_x \to \frac{q\,\lambda\,E_x}{m\,c^2}, \quad B_x \to \frac{q\,\lambda\,B_x}{m\,c}, \tag{3.1}$$

analogously for y and z components. As seen in Eqs. (2.4), the increment of particle momentum is a combination of that in the electric field, in the magnetic field and due to curvilinear acceleration. The integration procedure at every step τ is divided in the five stages. At each stage, integration schemes of the first order are used with neglected terms of the order of $o(\tau^2)$. They require calculation of the space charge field of the beam only once per integration step, which saves computational time.

A. At the first stage, the particle performs a half-step acceleration in the electric field

$$p^*_{x,n} = p_{x,n} + \frac{\tau}{2} E_{x,n}, \quad p^*_{y,n} = p_{y,n} + \frac{\tau}{2} E_{y,n}, \quad p^*_{z,n} = p_{z,n} + \frac{\tau}{2} E_{z,n}. \tag{3.2}$$

B. After that, the vector of the particle momentum accomplishes rotation in the magnetic field, utilizing an implicit centered scheme:

$$\frac{\vec{p}^*_{n+1} - \vec{p}^*_n}{\tau} = [\frac{(\vec{p}^*_{n+1} + \vec{p}^*_n)}{2\,\gamma^*_n} \times \vec{B}_n], \text{ or, in explicit form,} \tag{3.3}$$

$$\begin{vmatrix} p^*_{x,n+1} \\ p^*_{y,n+1} \\ p^*_{z,n+1} \end{vmatrix} = C \begin{vmatrix} [1+\frac{\tau^2}{(2\gamma^*_n)^2}(B^2_x-B^2_y-B^2_z)] & \tau(\frac{B_z}{\gamma^*_n}+B_xB_y\frac{\tau}{2(\gamma^*_n)^2}) & \tau(B_xB_z\frac{\tau}{2(\gamma^*_n)^2}-\frac{B_y}{\gamma^*_n}) \\ \tau(B_xB_y\frac{\tau}{2(\gamma^*_n)^2}-\frac{B_z}{\gamma^*_n}) & [1+\frac{\tau^2}{(2\gamma^*_n)^2}(B^2_y-B^2_x-B^2_z)] & \tau(\frac{B_x}{\gamma^*_n}+B_yB_z\frac{\tau}{2(\gamma^*_n)^2}) \\ \tau(\frac{B_y}{\gamma^*_n}+B_zB_x\frac{\tau}{2(\gamma^*_n)^2}) & \tau(B_yB_z\frac{\tau}{2(\gamma^*_n)^2}-\frac{B_x}{\gamma^*_n}) & [1+\frac{\tau^2}{(2\gamma^*_n)^2}(B^2_z-B^2_y-B^2_x)] \end{vmatrix} \begin{vmatrix} p^*_{x,n} \\ p^*_{y,n} \\ p^*_{z,n} \end{vmatrix}, \tag{3.4}$$

$$C = \frac{1}{1+(\frac{\tau}{2\gamma^*_n})^2(B^2_x+B^2_y+B^2_z)}. \tag{3.5}$$

C. At the third stage, the particle performs curvilinear acceleration. The value of p_y is conserved at this stage, $p^{**}_{y,\,n+1} = p^*_{y,\,n+1}$. The difference equations for radial and longitudinal momentum with curvilinear acceleration are

$$\frac{p^{**}_{x,\,n+1} - p^*_{x,n+1}}{\tau} = \frac{1}{\gamma^*_n(R_n+x_n)}(\frac{p^*_{z,\,n+1}+p^{**}_{z,\,n+1}}{2})^2, \tag{3.6}$$

$$\frac{p^{**}_{z,\,n+1} - p^*_{z,\,n+1}}{\tau} = -\frac{1}{\gamma^*_n(R_n+x_n)}(\frac{p^{**}_{z,\,n+1}+p^*_{z,\,n+1}}{2})(\frac{p^{**}_{x,\,n+1}+p^*_{x,\,n+1}}{2}). \tag{3.7}$$

Equations (3.6) and (3.7) are coupled. The increment of the radial and the longitudinal components of the particle momentum at this stage consists of several steps.

C.1. Advance of radial momentum:

$$p^{**}_{x,\,n+1} = p^*_{x,\,n+1} + \frac{(p^*_{z,\,n+1})^2}{\gamma^*_n\;(R_n + x_n)}\;\tau\;.$$ (3.8)

C.2. Advance of longitudinal momentum:

$$p^{**}_{z,\,n+1} = p^*_{z,\,n+1}\;\frac{1 - s\cdot(p^*_{x,\,n+1} + p^{**}_{x,\,n+1})}{1 + s\cdot(p^*_{x,\,n+1} + p^{**}_{x,\,n+1})}\;,\qquad\qquad s = \frac{\tau}{4\,\gamma^*_n\;(R_n + x_n)}\;.$$ (3.9)

C.3. Correction of radial momentum:

$$p^{**}_{x,\,n+1} = p^*_{x,\,n+1} + \frac{\tau}{\gamma^*_n\;(R_n + x_n)}\;(\frac{p^*_{z,\,n+1} + p^{**}_{z,\,n+1}}{2})^2\;.$$ (3.10)

The total momentum under curvilinear acceleration is conserved, as follows from Eqs. (2.4):

$$\frac{1}{2}\,d(p_x^2 + p_z^2) = p_x\,dp_x + p_z\,dp_z = (\,p_x\,\frac{p_z^2}{\gamma\,(R+x)} - p_z\,\frac{p_z p_x}{\gamma\,(R+x)}\,)\tau = 0\;.$$ (3.11)

To achieve reasonable accuracy in the conservation of momentum, the steps C.2 and C.3 are iteratively repeated 3-4 times.

D. At the fourth stage, the particle again performs a half-step acceleration in the electric field:

$$p_{x,n+1} = p^{**}_{x,n+1} + \frac{\tau}{2}\,E_{x,n}\;,\qquad p_{y,n+1} = p^{**}_{y,n+1} + \frac{\tau}{2}\,E_{y,n},\qquad p_{z,n+1} = p^{**}_{z,n+1} + \frac{\tau}{2}\,E_{z,n}\;.$$ (3.12)

E. At the final stage, the particle performs the advancing of position:

$$x_{n+1} = x_n + \tau\,\frac{p_{x,n+1}}{\gamma_{n+1}},\quad y_{n+1} = y_n + \tau\,\frac{p_{y,n+1}}{\gamma_{n+1}},\quad z_{n+1} = z_n + \tau\,\frac{p_{z,n+1}}{\gamma_{n+1}\,(1 + \frac{x_{n+1}}{R_n})}\;.$$ (3.13)

The scheme presented here accomplishes the general-purpose integration of the particle trajectories in 6-dimensional phase space. Let us consider some special important cases.

3.2. Particle motion in electric field

Many low energy injectors utilize electrostatic quadrupole lenses and radio-frequency quadrupole linacs. The reference orbit in such structures is a straight line $1/R = 0$ and the magnetic field is $\vec{B} = 0$. In this case the integrator is reduced to the following scheme:

$$\vec{p}_{n+1} = \vec{p}_n + \tau \vec{E}_n , \qquad \vec{x}_{n+1} = \vec{x}_n + \tau \frac{\vec{p}_{n+1}}{\gamma_{n+1}} . \qquad (3.14)$$

This scheme is symplectic, i.e. phase space volume is conserved [13]. Actually, the Jacobian of transformation from "old" variables, $\vec{x}_n$, $\vec{p}_n$, to "new" variables $\vec{x}_{n+1}$, $\vec{p}_{n+1}$ is equal to unity (for simplicity consider only the one-dimensional case, but the result is valid for the multi-dimensional case as well):

$$J = \begin{vmatrix} \dfrac{\partial x_{n+1}}{\partial x_n} & \dfrac{\partial x_{n+1}}{\partial p_n} \\ \dfrac{\partial p_{n+1}}{\partial x_n} & \dfrac{\partial p_{n+1}}{\partial p_n} \end{vmatrix} = \begin{vmatrix} 1 & 0 \\ \tau \dfrac{\partial E_{x,n}}{\partial x_n} & 1 \end{vmatrix} = 1 . \qquad (3.15)$$

At the same time, this scheme does not conserve the total energy of the particles [14]. For analysis consider the non relativistic case ($\gamma = 1$). The first of equations of (3.14) can be rewritten as

$$\vec{p}_{n+1} - \frac{\tau}{2} \vec{E}_n = \vec{p}_n + \frac{\tau}{2} \vec{E}_n . \qquad (3.16)$$

Square of both sides of Eq. (3.16) gives

$$\vec{p}_{n+1}^2 - \tau \vec{p}_{n+1} \vec{E}_n + \frac{\tau^2}{4} \vec{E}_n^2 = \vec{p}_n^2 + \tau \vec{p}_n \vec{E}_n + \frac{\tau^2}{4} \vec{E}_n^2 . \qquad (3.17)$$

Combination of Eq. (3.17) with the second equation of (3.14) is [14]

$$\frac{\vec{p}_{n+1}^2}{2} - \frac{\vec{p}_n^2}{2} = \vec{E}_n \left(\frac{\vec{x}_{n+1} - \vec{x}_{n-1}}{2} \right) . \qquad (3.18)$$

The left-side of Eq. (3.18) is the change of kinetic energy of the particle, while the right side is only an approximation of the change in potential energy:

$$\int_{x_n}^{x_{n+1}} \vec{E} \, d\vec{x} \approx \vec{E}_n \left(\frac{\vec{x}_{n+1} - \vec{x}_{n-1}}{2} \right) . \qquad (3.19)$$

For a one-dimensional harmonic oscillator $E_n = - \omega^2 x_n$, equation (3.18) becomes

$$p_{n+1}^2 + \omega^2 x_{n+1}^2 - \tau \omega^2 x_{n+1} p_{n+1} = p_n^2 + \omega^2 x_n^2 - \tau \omega^2 x_n p_n . \qquad (3.20)$$

In a harmonic oscillator the energy invariant is $E = p^2 + \omega^2 x^2$, whereas the application of a symplectic integrator results in the appearance of an additional term $- \tau \omega^2 x p$ [12]. Therefore, the symplectic integrator, Eq. (3.14), conserves energy up to the order of τ.

A more general theorem [12] states that the symplectic integrator of the m-th order describes the evolution of an associated Hamiltonian $\widetilde{H}$:

$$\widetilde{H} = H + \tau^m H_m + o\,(\tau^{m+1})\,, \tag{3.21}$$

where H is an original Hamiltonian and the other terms are

$$H_1 = \frac{1}{2} \frac{\partial H}{\partial p} \frac{\partial H}{\partial x}, \quad H_2 = \frac{1}{12} \left[\frac{\partial^2 H}{\partial p^2} \left(\frac{\partial H}{\partial x}\right)^2 + \frac{\partial^2 H}{\partial x^2} \left(\frac{\partial H}{\partial p}\right)^2 \right], \quad H_3 = \frac{1}{12} \frac{\partial^2 H}{\partial p^2} \frac{\partial^2 H}{\partial x^2} \frac{\partial H}{\partial p} \frac{\partial H}{\partial x}\,, \ldots \tag{3.22}$$

Eq. (3.21) indicates that the symplectic integrator corresponds to a physical system, which is slightly different from the original one. For an integrator of the first order, Eq. (3.14), the error in energy remains of the order of τ, which coincides with the estimation of Eq. (3.20). Meanwhile, if the integration step τ is small enough, the difference between the original Hamiltonian, H, and the associated Hamiltonian, $\widetilde{H}$, is not significant.

3.3. Particle motion in magnetic field

Consider the rotation of a particle in a uniform magnetic field $\vec{B} = \{0, 0,\ B_z\}$. The transformation from "old" variables to "new' variables is given by formulas (3.4), (3.13), which are reduced to the following scheme [14]:

$$p_{x,n+1} = p_{x,n} \frac{(1 - \Phi^2)}{1 + \Phi^2} + p_{y,n} \frac{2\,\Phi}{1 + \Phi^2}\,, \tag{3.23}$$

$$p_{y,n+1} = p_{y,n} \frac{(1 - \Phi^2)}{1 + \Phi^2} - p_{x,n} \frac{2\,\Phi}{1 + \Phi^2}\,, \quad \Phi = \frac{\tau\,B_z}{2\gamma}\,.$$

The transformation, Eq. (3.23), conserves the total momentum of the particle [11]:

$$p_{x,\ n+1}^2 + p_{y,\ n+1}^2 = p_{x,\ n}^2 + p_{y,\ n}^2\,, \tag{3.24}$$

which is essential, otherwise the particle trajectory would be unphysically swept into a spiral [14]. Also, phase space volume is conserved by Eqs. (3.23). But in an arbitrary magnetic field, the integrator (3.4), (3.13) is not symplectic. In general, mechanical momentum and particle coordinates, are not canonical - conjugate variables.

These examples demonstrate that for particle tracking it is necessary to find a reasonable compromise between the different properties of integration schemes. With the appropriate choice of the value of the integration step, τ, the beam parameters become insensitive to the variation of τ.

Usually the value of integration step with respect to RF period or plasma oscillation period is $\tau = 10^{-2} - 10^{-3}$, which is enough to insure good accuracy of the calculations.

4. SPIN MATRIX FORMALISM

The rotation of spin $\vec{S}$ of a particle with charge q, mass m, velocity $\vec{\beta} = \vec{v}/c$ and energy γ is described by the Bargmann-Michel-Telegdi (BMT) equation [15]:

$$\frac{d\vec{S}}{dt} = \frac{q}{m\gamma} \vec{S} \times [(1 + G\gamma)\vec{B}_\perp + (1+G)\vec{B}_{II} + (G\gamma + \frac{\gamma}{1+\gamma}) \frac{\vec{E} \times \vec{\beta}}{c}] , \qquad (4.1)$$

where G is an anomalous magnetic momentum of the particle, $\vec{E}$ is an electrical field, and $\vec{B}_\perp$ and $\vec{B}_{II}$ are components of magnetic field, perpendicular and parallel to particle velocity, respectively:

$$\vec{B}_\perp = \frac{1}{v^2} (\vec{v} \times \vec{B}) \times \vec{v} , \qquad (4.2)$$

$$\vec{B}_{II} = \frac{1}{v} (\vec{v} \cdot \vec{B}) \frac{\vec{v}}{v} . \qquad (4.3)$$

Assuming electromagnetic field is constant over a small distance δz, the solution of the BMT equation can be written in matrix form as [16]

$$\begin{vmatrix} S_x \\ S_y \\ S_z \end{vmatrix} = \begin{vmatrix} 1- a(B^2+C^2) & ABa + Cb & ACa - Bb \\ ABa -Cb & 1- a(A^2+C^2) & BCa + Ab \\ ACa + Bb & BCa - Ab & 1- a(A^2+B^2) \end{vmatrix} \begin{vmatrix} S_{x,o} \\ S_{y,o} \\ S_{z,o} \end{vmatrix} , \qquad (4.4)$$

$$A = \frac{P_x}{P_o}, \quad B = \frac{P_y}{P_o}, \quad C = \frac{P_z}{P_o}, \qquad (4.5)$$

$$a = 1 - \cos \varphi, \quad b = \sin \varphi, \quad \varphi = P_o \delta z , \qquad (4.6)$$

where parameters P_x, P_y, P_z are given by the following expressions:

$$P_x = \frac{q}{m\gamma v} [(1+G\gamma)(B_x - x' B_z) + (1+G)x'B_z + \frac{v}{c^2} (\frac{\gamma}{1+\gamma} + G\gamma)(E_y - y'E_z)] , \qquad (4.7)$$

$$P_y = \frac{q}{m\gamma v} [(1+G\gamma)(B_y - y' B_z) + (1+G)y'B_z + \frac{v}{c^2} (\frac{\gamma}{1+\gamma} + G\gamma)(x'E_z - E_x)] , \qquad (4.8)$$

$$P_z = \frac{q}{m\,\gamma\,v}\,[(1+G\gamma)(-x'\,B_x - y'\,B_y) + (1+G)(x'B_x+B_z + y'B_y) + \frac{v}{c^2}\,(\frac{\gamma}{1+\gamma} + G\gamma)(y'\,E_x - E_y x')]\ . \quad (4.9)$$

and prime means derivative over longitudinal coordinate, $' = d/dz$. Matrix equations (4.4) are integrated simultaneously with particle tracking.

Matrix (4.4) describes spin precession in Cartesian coordinates. If particle travels in a bending magnet, spin is corrected at every integration step according to the matrix

$$\begin{vmatrix} S_x \\ S_y \\ S_z \end{vmatrix} = \begin{vmatrix} \cos\theta & 0 & -\sin\theta \\ 0 & 1 & 0 \\ \sin\theta & 0 & \cos\theta \end{vmatrix} \begin{vmatrix} S_{x,o} \\ S_{y,o} \\ S_{z,o} \end{vmatrix} , \quad (4.10)$$

which describes rotation of system of coordinates for angle $\theta = -(z_{n+1} - z_n)/R_n$ at every integration step.

5 BEAM DISTRIBUTION GENERATOR IN PHASE SPACE

At the initial moment of time every particle occupies a starting position in 6-dimensional phase space depending on the specific particle distribution. In most cases the longitudinal distribution corresponds to a z - continuous beam with a finite spread of longitudinal momentum Δp_z. Simulation of longitudinal phase space for a z-uniform beam is performed as a generation of a uniform particle distribution within the interval $- \beta\lambda/2 \leq z \leq \beta\lambda/2$ and a Gaussian distribution in longitudinal momentum around the average value of $\bar{p}_z$:

$$\frac{dN}{dp_z} = \frac{N}{\sqrt{2\pi}\,\Delta p_z} \exp[- \frac{(p_z - \bar{p}_z)^2}{2(\Delta p_z)^2}] . \quad (5.1)$$

The generation of a bunched beam distribution in longitudinal phase space is described below, see Eq. (5.22).

For the simulation of particle distribution in transverse four-dimensional phase space x, x', y, y', consider a class of distributions with elliptical symmetry [17]. The distribution function f (x, x', y, y') depends on parameter F, which has a meaning for the value of the radius-vector in 4D phase space:

$$f (x, x',y, y') = \frac{dN}{dx\,dx'\,dy\,dy'} = f(F) , \quad (5.2)$$

$$F = \zeta_x^2 + v\zeta_y^2 , \quad (5.3)$$

where $v = \ni_x / \ni_y$ is a ratio of beam emittances. Parameters ζ_x, ζ_y describe a family of ellipses:

$$\zeta_{5x}^2 = (a_x x' - a_x' x)^2 + (\frac{x}{a_x})^2 \, , \qquad\qquad (5.4)$$

$$\zeta_{5y}^2 = (a_y y' - a_y' y)^2 + (\frac{y}{a_y})^2 \, , \qquad\qquad (5.5)$$

where a_x, a_x', a_y, a_y' are defined by the values of the semi-axes X_1, X_2, Y_1, Y_2 and tilts of the beam ellipses α_x, α_y at the phase planes, see Fig. 3, [18]:

$$a_x = \sqrt{\frac{X_1}{X_2} \cos^2\alpha_x + \frac{X_2}{X_1} \sin^2\alpha_x} \, , \qquad\qquad (5.6)$$

$$a_x' = \frac{1}{2\,a_x} (\frac{X_1}{X_2} - \frac{X_2}{X_1}) \sin 2\alpha_x \, , \qquad\qquad (5.7)$$

with analogous expressions for a_y, a_y'. The distribution function is normalized under condition:

$$\int_{-\infty}^{\infty} \int_{-\infty}^{\infty} \int_{-\infty}^{\infty} \int_{-\infty}^{\infty} f(x, x', y, y') \, dx \, dx' \, dy \, dy' = 1 \quad . \qquad\qquad (5.8)$$

Equation F = const defines a hyperellipsoid surface in phase space x, x', y, y'. From Eq. (5.2) it follows that phase space density is constant at the hyperellipsoid surface and varies from the surface to surface. For a fixed value of F, the projection of distribution, Eq. (5.2), at phase planes (x, x') , (y, y') are ellipses with unequal areas:

$$\zeta_{5x}^2 = F, \qquad\qquad \zeta_{5y}^2 = \frac{F}{\nu} \, . \qquad\qquad (5.9)$$

Different beam distributions are compared by root-mean-square (rms) values

$$<x^2> = \int_{-\infty}^{\infty} \int_{-\infty}^{\infty} \int_{-\infty}^{\infty} \int_{-\infty}^{\infty} x^2 \, f(x, x', y, y') \, dx \, dx' \, dy \, dy' \quad , \qquad\qquad (5.10)$$

with analogous expressions for $<x'^2>$, $<x\,x'>$, $<y^2>$, etc. The projection of the beam on phase plane (x, x') is described by an rms ellipse (see Fig. 3)

$$(\frac{4<x'^2>}{\mathfrak{z}_x})x^2 - 2\,(\frac{4<x\,x'>}{\mathfrak{z}_x})\,x\,x' + (\frac{4<x^2>}{\mathfrak{z}_x})x'^2 = \mathfrak{z}_x \, , \qquad\qquad (5.11)$$

with analogous expression for the plane (y, y'). The area of the rms ellipse is $\pi\mathfrak{z}_x$, where $\mathfrak{z}_x$ is a natural (non-normalized) rms beam emittance

$$\mathfrak{z}_x = 4 \sqrt{<x^2><x'^2> - <x\,x'>^2} \, . \qquad\qquad (5.12)$$

The problem of generating of particle distribution in phase space is to find 4N values x_i, x'_i, y_i, y'_i, $i = 1, 2,..., N$, which correspond to a given beam distribution function $f(F)$. The parameters for the rms ellipses X_1, X_2, α_x, Y_1, Y_2, α_y at phase planes (x, x'), (y, y') are initial data. To implement the algorithm, the distribution of values of F is required:

$$g\,(F) = \frac{d\,N(F)}{d\,F}\,,\tag{5.13}$$

where $dN(F)$ is the number of particles within the interval $(F, F + dF)$. To find the distribution $g(F)$, let us substitute new variables F, θ, φ, ψ $(0 \leq \theta \leq 2\pi,\ 0 \leq \varphi \leq 2\pi,\ 0 \leq \psi \leq \pi/2)$ for the old variables x, x', y, y' according to the following transformation:

$$a_x\,x' - a'_x\,x = \sqrt{F}\ \sin\psi\,\sin\varphi\,,$$

$$\frac{x}{a_x}\ = \sqrt{F}\,\sin\psi\,\cos\varphi\,,$$

$$\sqrt{\nu}\,(a_y\,y' - a'_y\,y) = \sqrt{F}\,\cos\psi\ \cos\theta\,,\tag{5.14}$$

$$\sqrt{\nu}\,\frac{y}{a_y}\ = \sqrt{F}\,\cos\psi\,\sin\theta\,.$$

The phase space element is transformed as

$$dx\,dx'\,dy\,dy' = \frac{1}{4\nu}\,F\,dF\,\sin 2\psi\,d\psi\,d\varphi\,d\theta\,.\tag{5.15}$$

Then the number of particles in the phase space element is

$$dN(F, \psi,\ \varphi,\ \theta) = f(F)\,\frac{1}{4\nu}\,F\,dF\,\sin 2\psi\,d\psi\,d\varphi\,d\theta\,.\tag{5.16}$$

Integration of Eq. (5.16) over the angle variables θ, ψ, φ gives the number of particles dN as a function of the value F:

$$dN(F) = f(F)\ \frac{1}{4\nu}\,F\,dF\int_0^{2\pi} d\varphi\int_0^{2\pi} d\theta\int_0^{\pi/2}\sin 2\psi\,d\psi = \frac{\pi^2}{\nu}\ f(F)\,F\,dF\,.\tag{5.17}$$

From Eq. (5.17) the distribution of the value F is

$$g\,(F) = \frac{\pi^2}{\nu}\ f(F)\,F\,.\tag{5.18}$$

The algorithm of particle generation in phase space is divided into three steps:

A. Calculation of the coefficients a_x, a'_x a_y, a'_y according to Eqs. (5.6), (5.7) using the given parameters for the rms ellipses X_1, X_2, α_x, Y_1, Y_2, α_y at the phase planes (x, x'), (y, y').

B. Generation of the distribution, g(F), using the inverse function method. For that an integral distribution of the value F is calculated

$$G(F) = \int_0^F g(F')\,dF' \ . \tag{5.19}$$

Then the inverse function F = F(G) is generated taking the value of G uniformly distributed in the interval (0, 1).

C. For each value of F, two random numbers ζ_x, ζ_y are taken, which satisfy Eq. (5.3). The values ζ_x, ζ_y, define two specific ellipses, Eqs. (5.4), (5.5) among a family of ellipses with fixed ratios of X_1/X_2, Y_1/Y_2 and angles α_x, α_y. On each ellipse an arbitrary point is taken with the following coordinates [18]:

$$x = \zeta_x\, a_x \cos \beta_x \ ,$$

$$x' = \xi_x\, (a'_x \cos \beta_x - \frac{\sin \beta_x}{a_x})\ ,$$

$$\tag{5.20}$$

$$y = \zeta_y\, a_y \cos \beta_y \ ,$$

$$y' = \zeta_y\, (a'_y \cos \beta_y - \frac{\sin \beta_y}{a_y})\ ,$$

where the values of β_x, β_y are randomly distributed within the intervals:

$$0 \le \beta_x \le 2\pi\ , \qquad 0 \le \beta_y \le 2\pi\ . \tag{5.21}$$

The values x, x', y, y' obtained from Eqs. (5.20) define the point in 4D phase space which belongs to distribution f(F). The steps B, C are repeated N times until N points fill in the phase space volume.

The method described is used in the program as the generator of the following initial distributions in phase space: KV, "water bag", parabolic, Gaussian. Definition and characteristics of such distributions are given in Table 2. For Gaussian distribution the random number generator, presented in Ref. [19] is used because the inverse function method, Eq. (5.19), is too slow in this case.

The same technique is used for the simulation of a bunched beam distribution in longitudinal phase space (z-z') utilizing an rms beam ellipse:

$$(\frac{4\langle z'^2\rangle}{\ni_z})z^2 - 2\,(\frac{4\langle z\,z'\rangle}{\ni_z})\,z\,z' + (\frac{4\langle z^2\rangle}{\ni_z})z'^{\,2} = \ni_z\ . \tag{5.22}$$

The results of simulation of different distributions are presented in Fig. 4 and in Table 3. The error of representation of the rms beam emittances by the generator which was developed is 10^{-2} - 10^{-4}. For each distribution, the error decreases approximately as $1/\sqrt{N}$, which is typical for filling up an area utilizing a random number generator.

6 CALCULATION OF ACCELERATING AND FOCUSING FIELDS

6.1. Electromagnetic field in RF gap

The field inside an RF gap is represented by the Fourier-Bessel series (see Fig. 5):

$$E_z(z,r,t) = - \cos(\omega t + \varphi_o) \sum_{m=1}^{M} E_m I_0(\mu_m r) \sin\left(\frac{2\pi mz}{L}\right),$$

$$E_r(z,r,t) = \cos(\omega t + \varphi_o) \sum_{m=1}^{M} E_m \frac{2\pi m}{\mu_m L} I_1(\mu_m r) \cos\left(\frac{2\pi mz}{L}\right),$$

$$(6.1)$$

$$B_\theta(z,r,t) = \frac{1}{c} \sin(\omega t + \varphi_o) \sum_{m=1}^{M} E_m \frac{2\pi}{\mu_m \lambda} I_1(\mu_m r) \sin\left(\frac{2\pi mz}{L}\right),$$

$$\mu_m = \frac{2\pi}{\lambda} \sqrt{\left(\frac{m\lambda}{L}\right)^2 - 1}.$$

The electrostatic field of axial-symmetric lenses is described by the formulas (6.1), assuming $\omega = 0$, $\varphi_o = 0$, and $\mu_m = \frac{2\pi m}{L}$. Two approaches to define the coefficients, E_m, of the series (6.1), are used in the program.

A. The field inside the gap is calculated separately utilizing an electrodynamics or electrostatic code. Coefficients E_m are derived from the aperture field distribution function $E_z(z_i, r=a)$ at the equidistant points $z_i = \frac{L}{2} \frac{i}{M}$:

$$E_z(z_i, a) = \sum_{m=1}^{M-1} E_m I_0(\mu_m a) \sin\left(\frac{\pi mi}{M}\right). \tag{6.2}$$

Multiplying equation (6.2) by $\sin\left(\frac{\pi m'i}{M}\right)$ and applying a discrete Fourier analysis, the coefficients are:

$$E_m = \frac{2}{M \cdot I_0(\mu_m a)} \sum_{i=1}^{M-1} E_z(z_i, a) \sin\left(\frac{\pi mi}{M}\right). \tag{6.3}$$

B. The longitudinal aperture field component $E_z(z, r=a)$ is assumed to be a step function of z (see Fig. 5):

$$E_z(a, z) = \begin{cases} 0, & 0 \le z \le \dfrac{l}{2} \\[2mm] E_o, & \dfrac{l}{2} \le z \le \dfrac{l}{2} + g \\[2mm] 0, & \dfrac{l}{2} + g \le z \le \dfrac{l}{2} + g + \dfrac{d}{2} \end{cases} \tag{6.4}$$

with anti-symmetric extension of the field at the next gap. The lengths of neighboring drift tubes are supposed to be unequal to each other, $l \ne d$. From the expansion, Eq. (6.1), the longitudinal field component at the aperture radius is:

$$E_z(a,z) = \sum_{m=1}^{M} E_m I_0(\mu_m a) \sin \left(\frac{2\pi m z}{L}\right) . \tag{6.5}$$

Multiplication the left and right sides of expression (6.5) by $\sin \left(\frac{2\pi m'z}{L}\right)$ and integration over period $L = l + d + 2g$ gives the following expression for Fourier-Bessel coefficients:

$$E_m = \frac{4 E_o}{I_0(\mu_m a)} \left[\frac{\pi m(l + g)}{L}\right] \left(\frac{g}{L}\right) \frac{\sin \left[\dfrac{\pi m(l + g)}{L}\right]}{\left[\dfrac{\pi m(l + g)}{L}\right]} \frac{\sin \left(\dfrac{\pi m g}{L}\right)}{\left(\dfrac{\pi m g}{L}\right)} . \tag{6.6}$$

In Fig. 6 an example of the field distribution in a gap using method B is presented. The number of Fourier harmonics in Eq. (6.1) depends on the process and typically is equal to $M = 5 - 10$.

6.2. Multipole lenses

Electric and magnetic fields of multipole lenses of the order n (n=2 for quadrupoles, n=3 for sextupoles, n=4 for octupoles, etc.) are represented as a step function in the z-direction with field components:

$$E_r = - E_o \left(\frac{r}{R_o}\right)^{n-1} \cos(n\theta + \theta_o) , \qquad\qquad B_r = - B_o \left(\frac{r}{R_o}\right)^{n-1} \cos(n\theta + \theta_o) ,$$

$$E_\theta = E_o \left(\frac{r}{R_o}\right)^{n-1} \sin(n\theta + \theta_o) , \qquad\qquad B_\theta = B_o \left(\frac{r}{R_o}\right)^{n-1} \sin(n\theta + \theta_o) , \tag{6.7}$$

where E_o, B_o are pole tip fields, R_o is a pole radius and θ_o is a skew angle. Another option available in the program is interpolation of the 3-dimensional grid function of the field components $\vec{B}(x_i, y_j, z_k), \vec{E}(x_i, y_j, z_k)$.

6.3. Axial-symmetric magnetostatic field

The magnetic field of solenoids and axial-symmetric permanent magnets is calculated as

$$B_z = B(z) - \frac{r^2}{4} \frac{d^2B}{dz^2} , \qquad B_r = -\frac{r}{2} \left(\frac{dB}{dz} - \frac{d^3B}{dz^3} \frac{r^2}{8} \right) , \qquad (6.8)$$

where the field at the axis $B(z)$ is given at fixed points. Another option available in the program is the interpolation of a 2-dimensional grid functions $B_z(z_i, r_j)$, $B_r(z_i, r_j)$.

6.4. Bending Magnets

The magnetic field inside a bending magnet is described by the Taylor expansion up to the terms of second order [20]:

$$B_x(x,y,z) = B_y \left(-n \frac{y}{R} + 2\xi \frac{xy}{R^2} \right) , \qquad (6.9)$$

$$B_y(x,y,z) = B_y \left[1 - n \frac{x}{R} + \frac{n}{2} \frac{y^2}{R^2} + \xi \frac{(x^2 - y^2)}{R^2} \right] , \qquad (6.10)$$

where B_y is the vertical component of magnetic field along the reference trajectory with radius of curvature R, n is the field index and ξ is a nonlinear coefficient in the magnetic field expansion:

$$n = - \left[\frac{R}{B_y} \frac{\partial B_y}{\partial x} \right]_{x=0,y=0} , \qquad \xi = \left[\frac{R^2}{2! \, B_y} \frac{\partial^2 B_y}{\partial x^2} \right]_{x=0,y=0} . \qquad (6.11)$$

At the entrance and at the exit of the magnet, the slope of the particle trajectory is changed because of the pole angle α according to the linear matrix transformation [20]:

$$\begin{vmatrix} x \\ x' \\ y \\ y' \end{vmatrix} = \begin{vmatrix} 1 & 0 & 0 & 0 \\ \dfrac{tg\alpha}{R} & 1 & 0 & 0 \\ 0 & 0 & 1 & 0 \\ 0 & 0 & -\dfrac{tg(\alpha - \psi)}{R} & 1 \end{vmatrix} \begin{vmatrix} x_o \\ x'_o \\ y_o \\ y'_o \end{vmatrix} . \qquad (6.12)$$

The correction angle ψ is given by the expression [21]

$$\psi = K_1 \left(\frac{g}{R} \right) \left(\frac{1 + \sin^2\alpha}{\cos\alpha} \right) \left[1 - K_1 K_2 \left(\frac{g}{R} \right) tg\alpha \right] , \qquad (6.13)$$

where g is the gap of the magnet and coefficients K_1, K_2 are defined by pole geometry.

6.5. Radio Frequency Quadrupole Structure (RFQ)

The acceleration of ions in an RFQ linac is performed in a four-vane structure modulated in the z-direction with the spatial period of $L = \beta\lambda$. The RFQ field in the i-th cell of the structure is given by [18]:

$$E_x = \frac{U_L}{a} \left[\chi \frac{x}{a} + (-1)^i \, 4T \, I_1(\mu_1 r) \, \left(\frac{a}{\beta\lambda}\right) \left(\frac{x}{r}\right) \sin(\mu_1 z) \right] \cos(\omega t + \varphi_o) , \qquad (6.14)$$

$$E_y = \frac{U_L}{a} \left[-\chi \frac{y}{a} + (-1)^i \, 4T \, I_1(\mu_1 r) \, \left(\frac{a}{\beta\lambda}\right) \left(\frac{y}{r}\right) \sin(\mu_1 z) \right] \cos(\omega t + \varphi_o) , \qquad (6.15)$$

$$E_z = 4 \frac{U_L}{\beta\lambda} (-1)^i \, T \, I_o(\mu_1 r) \cos(\mu_1 z) \cos(\omega t + \varphi_o) , \qquad \mu_1 = \frac{2\pi}{\beta\lambda} , \qquad (6.16)$$

where U_L is the potential difference between the electrodes, a is the aperture of the channel, χ is the focusing efficiency and T is the acceleration efficiency of the structure.

6.6 Accelerating waveguide

Analysis of particle acceleration in waveguide is performed in approximation that particles interact with the fundamental mode of disk-loaded waveguide with field components:

$$E_z = E_o \, e^{-\alpha z} \, I_o\left(\frac{2\pi r}{\beta\lambda\gamma}\right) \cos\varphi , \qquad (6.17)$$

$$E_r = -\gamma E_o \, e^{-\alpha z} \, I_1\left(\frac{2\pi r}{\beta\lambda\gamma}\right) \sin\varphi , \qquad (6.18)$$

$$B_\theta = \frac{\beta\gamma}{c} E_o \, e^{-\alpha z} \, I_1\left(\frac{2\pi r}{\beta\lambda\gamma}\right) \sin\varphi , \qquad (6.19)$$

where α is a waveguide attenuation, φ is a phase of particle in RF field

$$\varphi = 2\pi \frac{(\bar{z} - z_i)}{\beta\lambda} + \varphi_s , \qquad (6.20)$$

φ_s is a synchronous phase and $\bar{z}$ is a coordinate of the front of RF wave:

$$\bar{z} = z_o + \int_o^t \bar{\beta}(t') c \, dt' . \qquad (6.21)$$

Beam loading effect is expressed as superposition of longitudinal, W_z, and transverse, W_t, wake fields acting at every particle from other particles. Longitudinal wake fields are added to longitudinal component of electric field, E_z, while transverse wake fields are added to transverse components of Lorentz force, $\vec{F}_\perp = \vec{E}_\perp + [\vec{v} \times \vec{B}]_\perp$:

$$E_z(x, y, z) = - q \sum_{i=1}^{N} W_z(z - z_i),$$

$$F_x(x, y, z) = q \sum_{i=1}^{N} x_i \cdot W_t(z - z_i), \qquad (6.22)$$

$$F_y(x, y, z) = q \sum_{i=1}^{N} y_i \cdot W_t(z - z_i),$$

where summation is performed over particles with $z_i > z$. Wakefields are calculated separately and tabulated inside program.

7 POISSON'S SOLVERS

The space charge potential of the beam U_b for an instantaneous space charge density distribution, ρ, is calculated from the solution of Poisson's equation in a moving system of coordinates:

$$\Delta U_b = - \frac{\rho}{\varepsilon_o} . \qquad (7.1)$$

Calculations are performed for beams propagating along straight line, neglecting curvature of the beam. It is correct for the beam with transverse sizes much smaller than radius of curvature. For calculations, three kinds of symmetry are used:
- z - uniform beam (2-dimensional problem in x-y coordinates),
- axial-symmetric bunches (2-dimensional problem in r-z coordinates),
- bunches with transverse quadrupole symmetry (3-dimensional problem in x-y-z coordinates).

Utilizing symmetry in space charge density distributions results in a savings of the required computer time and memory. Due to the quasi-periodic formation of bunches in RF accelerators, it is possible to consider the motion of only one bunch. Space charge fields of neighboring bunches are taken into account by imposing periodic boundary conditions for potential and space charge density in the longitudinal direction.

For numerical calculations it is convenient to utilize dimensionless variables. Taking the dimensionless potential as $U = U_b \, q/(mc^2)$ and the dimensionless coordinates as in Eq. (3.1), Poisson's equation is written as

$$\Delta U = - Q, \qquad (7.2)$$

where Q is a dimensionless space charge density of the beam:

$$Q = \frac{\rho \, \lambda^2 \, q}{\varepsilon_o \, m \, c^2} \quad . \tag{7.3}$$

In Poisson's solver three stages are distinguished:

  - the distribution of space charge of macroparticles among grid nodes,
  - the solution of Poisson's equation on a grid,
  - the differentiation of the potential grid function to determine the components of electrostatic field in the moving system E_x', E_y', E_z'.

After that, a transformation into the laboratory system of coordinates is performed according to the Lorentz transformation:

$$E_x = \gamma \, E_x', \qquad E_y = \gamma \, E_y', \qquad E_z = E_z' \, . \tag{7.4}$$

Finally, the transverse components of electric field are multiplied by the factor of γ^{-2} to include the effect of the self magnetic field produced by the beam:

$$E_x - v_z \, B_y = \frac{E_x}{\gamma^2}, \qquad E_y + v_z \, B_x = \frac{E_y}{\gamma^2} \, . \tag{7.5}$$

7.1. Numerical errors and conservation law

The important aspect of numerical simulations is the balance between accuracy and the required resources of the computer to get an efficient solution for the problem. Control of accuracy is required because the solution itself is unknown in advance. To attain good accuracy, the number of macroparticles per cell has to be large enough, and the mesh size has to be much smaller than the beam size. But even if these conditions are fulfilled, the following errors are unavoidable: (i) errors caused by the discrete charge representation used in the macroparticle method, (ii) errors caused by the approximation formulas used in place of the exact derivatives of the Poisson's equation; (iii) errors of differentiation of the potential function to obtain values of electric field components, and (iv) computer round-off errors.

For Poisson's equation the Gauss theorem is valid:

$$\int_s \vec{E} \, d\vec{S} = \int_v Q \, dv \, . \tag{7.6}$$

To control errors of calculations, the following parameter can be used

$$\vartheta = 1 - \left| \frac{\displaystyle\int_S \vec{E}\, d\vec{S}}{\displaystyle\int_\upsilon Q\, d\upsilon} \right| , \qquad (7.7)$$

which has a meaning of error of the Gauss theorem. It is clear, that in exact calculations parameter $\vartheta = 0$. In Eq. (7.7) the denominator is equal to the total charge of the beam, which is known exactly and does not depend on the numerical method. The numerator in Eq. (7.7) depends on the solution of the Poisson's equation and includes all of the errors of space charge calculations. Control of parameter ϑ, Eq. (7.7), gives an integral numerical error. Since the Gauss theorem does not provide information about the fluctuation of the solution in details, an extra criteria like averaged deviation from the exact solution is required. Below we consider numerical technique and typical value of the error in the numerical solution of Poisson's equation in different coordinate systems.

In particle-in-cell simulation the errors in space charge forces are of random character. It results in an unphysical increase of effective beam emittance, even when a symplectic integrator is used. To establish a quantitative measure of this effect on beam dynamics, consider the linear oscillator $\ddot{x} + \omega^2 x = 0$, affected by random errors in space charge field calculations. The matrix for the particle transformation in coordinates $(x, p = \frac{1}{\omega}\frac{dx}{dt})$ at every elementary step, δt, is given by

$$\begin{pmatrix} x_{n+1} \\ p_{n+1} \end{pmatrix} = \begin{pmatrix} \cos\theta & \sin\theta \\ -\sin\theta & \cos\theta \end{pmatrix} \begin{pmatrix} x_n \\ p_n + \Delta p_n \end{pmatrix} , \qquad (7.8)$$

where $\theta = \omega\, \delta t$ is a tune shift of particle oscillation per integration step and Δp_n is a random kick due to error δE_n in space charge field:

$$\Delta p_n = \frac{q\, \delta E_n\, \delta t}{m\, \omega} . \qquad (7.9)$$

For a circular beam of radius R, the error of Gauss theorem, ϑ, Eq. (7.7), is

$$\vartheta = \frac{\delta E(R)}{E(R)} , \qquad (7.10)$$

where E(R) is an exact value of the space charge field at the beam boundary:

$$E(R) = \frac{I}{2\pi\varepsilon_o\beta_z cR} , \qquad (7.11)$$

and $\delta E(R)$ is the deviation of space charge field from the value of $E(R)$. The solution of matrix equation (7.8) after n steps of integration is [22]

$$x_n = R \cos (n\theta + \Psi) + \sum_{i=0}^{n-1} \Delta p_i \sin (n-i)\, \theta$$

$$p_n = - R \sin (n\theta + \Psi) + \sum_{i=0}^{n-1} \Delta p_i \cos (n-i)\, \theta \tag{7.12}$$

where Ψ is the initial phase of oscillations. The root mean square values of the particle positions in phase space are

$$<x_n^2> = \frac{1}{2\pi} \int_{-\pi}^{\pi} x_n^2 \, d\Psi, \qquad <p_n^2> = \frac{1}{2\pi} \int_{-\pi}^{\pi} p_n^2 \, d\Psi \ . \tag{7.13}$$

Random kicks Δp_i are not correlated, therefore

$$\Delta p_k \sin (n-k)\theta \sum_{i=0}^{n-1} \Delta p_i \sin (n-i)\theta = \left\{ \begin{array}{ll} 0, & k \neq i \\ \Delta p^2 \sin^2(n-k)\theta, & k = i \end{array} \right. , \tag{7.14}$$

where Δp is the amplitude of a random kick. After n steps, the rms values are

$$<x_n^2> = \frac{R^2}{2} \left[1 + \left(\frac{\Delta p}{R}\right)^2 n \right], \qquad <p_n^2> = \frac{R^2}{2} \left[1 + \left(\frac{\Delta p}{R}\right)^2 n \right] . \tag{7.15}$$

Therefore, the normalized beam emittance after n steps, $\varepsilon_n = 4 \sqrt{<x_n^2><p_n^2>}$, is related to initial emittance, ε_o, as

$$\frac{\varepsilon_n}{\varepsilon_o} = 1 + \left(\frac{\Delta p}{R}\right)^2 n \ . \tag{7.16}$$

Let us rewrite the value of kick, Eq.(7.9), as

$$\Delta p = \frac{q}{m\omega} \left(\frac{\delta E}{E}\right) \left(\frac{\delta t}{T}\right) E\, T \ , \tag{7.17}$$

where $T = 2\pi/\omega$ is a period of the oscillations. Also take into account that the natural beam emittance is

$$\ni = \frac{R^2\, \omega}{\beta_z c} \ . \tag{7.18}$$

Therefore, the amplitude of the random kick is

$$\Delta p = 2\pi R \left(\frac{\delta E}{E}\right)\left(\frac{\delta t}{T}\right)\frac{2I}{I_c \beta_z^3}\frac{R^2}{\textэ^2}\ , \tag{7.19}$$

where $I_c = 4\pi\varepsilon_o m_o c^3/q = A/Z\cdot 3.13\cdot 10^7$ amp is a characteristic value of the beam current. The following combination of parameters

$$b = \frac{2I}{I_c \beta_z^3}\frac{R^2}{\textэ^2}\ , \tag{7.20}$$

is the ratio of beam brightness, $I/\textэ^2$, to the normalization value, I_c/R^2, and can be called the dimensionless beam brightness. Space charge dominated beam transport is performed when $b \gg 1$ while the emittance dominated regime is characterized by $b \ll 1$. Finally, beam emittance growth due to random variations in space charge field calculations is

$$\frac{\varepsilon_n}{\varepsilon_o} = 1 + \left(2\pi\, b\, \tau\, \frac{\delta E}{E}\right)^2 n\ , \tag{7.21}$$

where $\tau = \delta t/T$ is the dimensionless integration step. From Eq. (7.21) it follows that emittance growth is the most essential for high brightness beams. In Fig. 7a an example of beam emittance growth due to errors in space charge field calculations is presented. After 9000 integration steps emittance growth for the KV beam with $A/Z = 1$, $I = 4.16$ amp, $R = 1$ mm, $\beta_z = 0.015648$, $\textэ = 6.39\ \pi$ cm mrad, $b = 17$, $\delta E(R)/E(R) = 0.01$ is $\varepsilon_n/\varepsilon_o = 1.025$. Beam was represented by $3\cdot 10^4$ particles on the grid $N_x \times N_y = 512 \times 512$. Analytical estimation of beam emittance growth utilizing formula (7.21) gives $\varepsilon_n/\varepsilon_o = 1.1$. Without space charge forces the effective beam emittance is conserved (see Fig. 7b).

Let us note that rms beam emittance growth, presented in Fig. 7a and described by Eq. (7.21), does not violate Liouville's theorem, because it is growth of the effective phase space area occupied by the beam. Both the numerical integrator, Eq. (3.14) and matrix, Eq.(7.8), are symplectic, i.e. conserving microscopic phase space of the beam. Effective beam emittance can be increased while microscopic emittance is conserved (see for example, Ref. [23], Fig. 4.8, page 198). Fig. 8 illustrates evolution of phase space area occupied by the beam. Without space charge forces beam boundary in phase space remains unchanged. With space charge forces beam boundary is distorted due to random fluctuations in space charge field, which results in increase of effective phase space area. Meanwhile, microscopic phase space area and number of particles inside the area are conserved.

7.2. Particle weighting on a multidimensional grid

The region occupied by ensemble of particles is divided into uniform rectangular meshes of dimension $N_x \cdot N_y$, $N_z \cdot N_r$ or $N_x \cdot N_y \cdot N_z$ (see Fig. 9). Charge of every particle with coordinates (x_n, y_n), (r_n, z_n) or (x_n, y_n, z_n) is distributed among the nearest four (2D problem) or eight (3D problem) nodes. Every node receives contribution from charge of an individual particle utilizing area weighting method (see Figs. 10, 11). The charge density at node points, $Q_{i, j}$, $Q_{k, j}$, $Q_{i, j, k}$ is a combination of contributions from all particles which are inside the given elementary mesh:

$$Q_{i,j} = \sum_{n=1}^{N} Q_{xy} \, (1-\frac{|x_n - x_i|}{h_x}) \, (1-\frac{|y_n - y_j|}{h_y}) \,, \quad \text{x-y problem,} \tag{7.22}$$

$$Q_{k,j} = \sum_{n=1}^{N} Q_{rz} \, (1-\frac{|r_n - r_j|}{h_r}) \, (1-\frac{|z_n - z_k|}{h_z}) \,, \quad \text{r-z problem,} \tag{7.23}$$

$$Q_{i,j,k} = \sum_{n=1}^{N} Q_{xyz} \, (1-\frac{|x_n - x_i|}{h_x}) \, (1-\frac{|y_n - y_j|}{h_y}) \, (1-\frac{|z_n - z_k|}{h_z}) \,, \quad \text{x-y-z problem,} \tag{7.24}$$

where Q_{xy}, Q_{rz}, Q_{xyz} are dimensionless space charge density of individual particle and h_x, h_y, h_r, h_z are mesh sizes.

Beam of transported particles has a current of $I = \overline{Q_l} \, \beta c$, where Q_l is a beam charge per unit length. In grid weighting method, Eq. (7.22), one particle occupies area of $h_x \cdot h_y$. Space charge density of individual particle is $Q_l /(N \, h_x \, h_y)$. Dimensionless space charge density of individual particle in Eq. (7.22) is given by

$$Q_{xy} = \frac{Q_l}{N \, h_x \, h_y} \, \frac{\lambda^2 \, q}{\varepsilon_o \, m \, c^2} = \frac{4 \, \pi}{\beta N} \, \frac{I}{I_c} \, \frac{\lambda^2}{h_x \, h_y} \,. \tag{7.25}$$

Current of bunched beam is $I = Q_{bunch} / T$, where Q_{bunch} is a charge of one bunch and $T = \lambda/c$ is a RF period. Therefore, space charge densities of individual particle in Eqs. (7.23), (7.24) are

$$Q_{rz} = \frac{1}{N} \, \frac{Q_{bunch}}{2\pi r \, h_r \, h_z} \, \frac{\lambda^2 \, q}{\varepsilon_o \, mc^2} = \frac{2}{N} \, \frac{I}{I_c} \, \frac{\lambda^3}{r_j \, h_r \, h_z} \,, \tag{7.26}$$

$$Q_{xyz} = \frac{1}{N} \, \frac{Q_{bunch}}{h_x \, h_y \, h_z} \, \frac{\lambda^2 \, q}{\varepsilon_o \, mc^2} = \frac{4\pi}{N} \, \frac{I}{I_c} \, \frac{\lambda^3}{h_x h_y h_z} \,, \tag{7.27}$$

where $r_j = (j-1) \, h_r$ is a radius of j-th node.

Utilization of grid and distribution of charge of every particle among grid nodes is equivalent to charged clouds model instead of point charges model. It results in smoothing of particle distribution and suppression of particle-particle collisions in the model.

7.3. Space charge solver in 2D Cartesian coordinates

Space charge field of a z-uniform beam is calculated from the Poisson's equation in two-dimensional Cartesian coordinates

$$\frac{\partial^2 U}{\partial x^2} + \frac{\partial^2 U}{\partial y^2} = - Q\,(x,y), \qquad U(\Gamma) = 0 \,, \tag{7.28}$$

with Dirichlet boundary condition for potential U at the surface Γ of an infinite pipe with rectangular cross section of a x b (see Fig. 9a). Unknown potential of the beam and space charge density at grid points are represented as Fourier series:

$$U_{ij} = \sum_{n=1}^{N_x-1} \sum_{m=1}^{N_y-1} \overline{U}_{nm} \sin(\frac{\pi ni}{N_x}) \sin(\frac{\pi mj}{N_y}), \tag{7.29}$$

$$Q_{ij} = \sum_{n=1}^{N_x-1} \sum_{m=1}^{N_y-1} \overline{Q}_{nm} \sin(\frac{\pi ni}{N_x}) \sin(\frac{\pi mj}{N_y}) \,. \tag{7.30}$$

As a first step, Fourier coefficients in space charge density expansion (7.30) are calculated:

$$\overline{Q}_{nm} = \frac{4}{N_x\, N_y} \sum_{i=1}^{N_x-1} \sum_{j=1}^{N_y-1} Q_{ij} \sin(\frac{\pi ni}{N_x}) \sin(\frac{\pi mj}{N_y}) \,. \tag{7.31}$$

Calculations are performed utilizing standard routines for Fast Fourier Transformation REALFT, FOUR1, SINFT [24]. Substitution of expansions (7.29), (7.30) into Poisson's equation (7.28) provides algebraic relationship between Fourier coefficients of space charge, $\overline{Q}_{nm}$, and potential, $\overline{U}_{nm}$:

$$\overline{U}_{nm} = \frac{\overline{Q}_{nm}}{(\frac{\pi n}{a})^2 + (\frac{\pi m}{b})^2} \,. \tag{7.32}$$

Calculation of Fourier coefficients, Eq. (7.32), is a second step in solution of Poisson's equation. At the third step the space charge potential is calculated utilizing expansion (7.29). Components of electrostatic field are found by differentiation of potential grid function:

$$E_x = - \frac{U_{i+1,j} - U_{i-1,j}}{2h_x} \,, \tag{7.33}$$

$$E_y = - \frac{U_{i,j+1} - U_{i,j-1}}{2h_y} \,. \tag{7.34}$$

In Table 4 results of test problem for different values of grid points, $N_g = N_x \cdot x \ N_y$, are presented. Initial values of space charge density were generated randomly in two directions within the interval of (0, 1). The value of error of the Gauss theorem, ϑ, was averaged after 10^4 different realizations of random initial data. As seen, error has a value of 10^{-2} ...10^{-4} and drops inversely proportional to the number of grid points, $\vartheta \sim N_g^{-1}$.

7.4. Space charge solver in 2D cylindrical coordinates

Space charge field of the train of axial-symmetric bunches is calculated from the Poisson's equation in two-dimensional cylindrical coordinates:

$$\frac{1}{r} \frac{\partial}{\partial r} (r \frac{\partial U}{\partial r}) + \frac{\partial^2 U}{\partial z^2} = - Q(r,z) \ , \tag{7.35}$$

with Dirichlet boundary conditions at the surface of the tube of radius a, Neumann condition at the axis and periodic condition in z-direction (see Fig. 9b):

$$U(a,z) = 0 \ , \quad \frac{\partial U}{\partial r}(0, z) = 0 \ , \quad U(r,z) = U(r,z + L) \ , \quad L = \overline{\beta\lambda} \ . \tag{7.36}$$

Poisson's equation (7.35) is substituted by finite-difference analog:

$$U_{k, j+1}(1 + \frac{1}{2(j-1)}) - 2U_{k, j}(1 + \frac{h_r^2}{h_z^2}) + U_{k, j-1}(1 - \frac{1}{2(j-1)})$$

$$+ U_{k+1, j} (\frac{h_r}{h_z})^2 + U_{k-1, j} (\frac{h_r}{h_z})^2 = - Q_{k,j} \ h_r^2 \ . \tag{7.37}$$

The first step of solution of Poisson's equation is Fourier expansion of unknown potential and space charge density in z-direction

$$U_{k,j} = \sum_{m=1}^{N_z} \overline{U}_m(j) \exp(- i \frac{2\pi (k-1)(m-1)}{N_z}) \ , \tag{7.38}$$

$$Q_{k,j} = \sum_{m=1}^{N_z} \overline{Q}_m(j) \exp(- i \frac{2\pi (k-1)(m-1)}{N_z}) \ . \tag{7.39}$$

Coefficients of Fourier expansion are defined by inverse Fourier transform:

$$\overline{U}_m(j) = \frac{1}{N_z} \sum_{k=1}^{N_z} U_{kj} \exp (i \frac{2\pi (k-1)(m-1)}{N_z}) \ , \tag{7.40}$$

$$\overline{Q}_m(j) = \frac{1}{N_z} \sum_{k=1}^{N_z} Q_{kj} \exp\left(i \frac{2\pi \, (k-1) \, (m-1)}{N_z}\right) . \tag{7.41}$$

Substitution of expansion (7.40), (7.41) into finite-difference analog of the Poisson's equation (7.37) results in a three-diagonal matrix equation:

$$\alpha_j \, \overline{U}_m(j+1) + \beta_j \, \overline{U}_m(j) + \gamma_j \, \overline{U}_m(j-1) = w_j, \qquad m = 1,....N_z, \tag{7.42}$$

$$w_j = - \overline{Q}_m (j) \, h_r^2 , \tag{7.43}$$

with matrix coefficients:

$$\alpha_j = 1 + \frac{1}{2(j-1)} , \qquad \beta_j = - 2[1+2(\frac{h_r}{h_z} \sin\frac{\pi m}{N_z})^2], \qquad \gamma_j = 1 - \frac{1}{2(j-1)} . \tag{7.44}$$

Matrix equation (7.42) is solved utilizing the run method [14]. Solution is represented in a recurrent form, when unknown value of $\overline{U}_m(j+1)$ is defined via known value of $\overline{U}_m(j)$ as:

$$\overline{U}_m(j+1) = \overline{U}_m(j) \, X_j + Y_j , \tag{7.45}$$

where X_j, Y_j, $j = 1, .. \, N_r - 1$ are auxiliary vectors. Substitution of Eq.(7.45) into Eq. (7.42) provides the following recurrent expressions for X_j, Y_j :

$$X_{j-1} = - \frac{\gamma_j}{\alpha_j \, X_j + \beta_j} , \qquad Y_{j-1} = \frac{w_j - \alpha_j \, Y_j}{\alpha_j \, X_j + \beta_j} . \tag{7.46}$$

Initial values of $X_{N_r - 1}$, $Y_{N_r - 1}$ are defined by Dirichlet boundary condition at the surface of the tube $X_{N_r - 1} = 0$, $Y_{N_r - 1} = \overline{U}_m(N_r)$. Then recurrent expressions (7.46) are used to determine the values of X_j, Y_j, from the top of the grid, $j = N_r - 1$, to the bottom, $j = 1$, for every value of m (straight run). Neumann boundary condition at the axis is used to define the first value of potential coefficient

$$\frac{\overline{U}_m(2) - \overline{U}_m(1)}{h_r} = 0 , \qquad \overline{U}_m(1) = \frac{Y_1}{1 - X_1} . \tag{7.47}$$

Other coefficients $\overline{U}_m(j)$, $j = 1,.... \quad N_r - 2$ are found from recurrent expression, Eq. (7.45) (inverse run). It gives the solution of three-diagonal matrix equation, Eq. (7.42). After that, the potential at grid points is calculated using Fourier series (7.38). Components of electrostatic field are calculated via differentiation of potential function (7.33), (7.34).

In Table 5 results of numerical solution of Poisson's equation for axial-symmetric bunch with Gaussian distribution

$$\rho = \frac{1}{(2\pi)^{3/2}\,\sigma^2\,\sigma_z}\,\exp\left(-\frac{x^2+y^2}{2\sigma^2}-\frac{z^2}{2\sigma_z^2}\right), \qquad (7.48)$$

with ratio of semi-axes $\sigma/\sigma_z =1/4$ are presented. Potential and components of electrostatic field of the Gaussian bunch in free space are given by [25]

$$U_b = \int_0^\infty \frac{d\,q}{4\pi^{3/2}\varepsilon_o(2\sigma^2+q)\sqrt{(2\sigma_z^2+q)}}\,\exp\left[-\frac{x^2+y^2}{(2\sigma^2+q)}-\frac{z^2}{(2\sigma_z^2+q)}\right], \qquad (7.49)$$

$$E_x = -x\int_0^\infty \frac{d\,q}{2\pi^{3/2}\varepsilon_o(2\sigma^2+q)^2\sqrt{(2\sigma_z^2+q)}}\,\exp\left[-\frac{x^2+y^2}{(2\sigma^2+q)}-\frac{z^2}{(2\sigma_z^2+q)}\right], \qquad (7.50)$$

analogously for E_y, E_z. In every point, numerical solution, $\vec{E}_{numer}^{(n)}(r,z)$, is different from the exact one, $\vec{E}_{analyt}^{(n)}(r,z)$. To exclude the effect of boundary conditions, the aperture size was chosen to be $a=5\sigma$ and the period was selected as $L = 10\sigma_z$. The accumulated error among all particles, normalized at the maximum value of space charge field, $\vec{E}_{max}$, gives an averaged error (see Table 5):

$$\delta = \frac{1}{N}\sum_{n=1}^{N}\left(\frac{\left|\vec{E}_{numer}^{(n)}(r,z)\right| - \left|\vec{E}_{analyt}^{(n)}(r,z)\right|}{\left|\vec{E}_{max}\right|}\right). \qquad (7.51)$$

In the considered case the error, δ, is within the interval of $10^{-2} - 10^{-3}$.

7.5. Space charge solver in 3D Cartesian coordinates

Space charge field of the bunched beam with 3D quadrupole symmetry is calculated from solution of the Poisson's equation in three-dimensional Cartesian coordinates (see Fig. 9c):

$$\frac{\partial^2 U}{\partial x^2} + \frac{\partial^2 U}{\partial y^2} + \frac{\partial^2 U}{\partial z^2} = -Q(x, y, z), \qquad (7.52)$$

with Dirichlet boundary condition for potential U at the surface of a rectangular pipe, periodic conditions in longitudinal direction and conditions for quadrupole symmetry:

$$U(0, y, z) = U(a, y, z) = U(x, 0, z) = U(x, b, z) = 0,$$

$$U(r, \theta, z) = U(r, -\theta, z),$$

$$U(r, \theta, z) = U(r, \theta + \pi, z),$$ (7.53)

$$U(x, y, z) = U(x, y, z+L).$$

The problem is solved in the half of domain $0 \le x \le a/2$. It saves computer memory and CPU time, but restricts our study by on-axis beams with quadrupole-symmetric cross section. The method of solution of Poisson's equation is based on 3D Fast Fourier Transform [26].

Unknown potential and space charge density functions are represented as Fourier series:

$$U_{ijk} = \frac{1}{2} \sum_{n=1}^{N_x-1} \sum_{m=1}^{N_y-1} \overline{U}_{mno}^{(c)} \sin\left(\frac{\pi ni}{N_x}\right) \sin\left(\frac{\pi mj}{N_y}\right) +$$

$$\sum_{n=1}^{N_x-1} \sum_{m=1}^{N_y-1} \sum_{l=1}^{\frac{1}{2}N_z-1} \left[\overline{U}_{mnl}^{(c)} \sin\left(\frac{\pi ni}{N_x}\right) \sin\left(\frac{\pi mj}{N_y}\right) \cos\left(\frac{2\pi kl}{N_z}\right) + \overline{U}_{mnl}^{(s)} \sin\left(\frac{\pi ni}{N_x}\right) \sin\left(\frac{\pi mj}{N_y}\right) \sin\left(\frac{2\pi kl}{N_z}\right)\right]$$

$$+ \frac{(-1)^k}{2} \sum_{n=1}^{N_x-1} \sum_{m=1}^{N_y-1} \overline{U}_{mn\frac{N_z}{2}}^{(c)} \sin\left(\frac{\pi ni}{N_x}\right) \sin\left(\frac{\pi mj}{N_y}\right),$$ (7.54)

$$Q_{ijk} = \frac{1}{2} \sum_{n=1}^{N_x-1} \sum_{m=1}^{N_y-1} \overline{Q}_{mno}^{(c)} \sin\left(\frac{\pi ni}{N_x}\right) \sin\left(\frac{\pi mj}{N_y}\right) +$$

$$\sum_{n=1}^{N_x-1} \sum_{m=1}^{N_y-1} \sum_{l=1}^{\frac{1}{2}N_z-1} \left[\overline{Q}_{mnl}^{(c)} \sin\left(\frac{\pi ni}{N_x}\right) \sin\left(\frac{\pi mj}{N_y}\right) \cos\left(\frac{2\pi kl}{N_z}\right) + \overline{Q}_{mnl}^{(s)} \sin\left(\frac{\pi ni}{N_x}\right) \sin\left(\frac{\pi mj}{N_y}\right) \sin\left(\frac{2\pi kl}{N_z}\right)\right]$$

$$+ \frac{(-1)^k}{2} \sum_{n=1}^{N_x-1} \sum_{m=1}^{N_y-1} \overline{Q}_{mn\frac{N_z}{2}}^{(c)} \sin\left(\frac{\pi ni}{N_x}\right) \sin\left(\frac{\pi mj}{N_y}\right).$$ (7.55)

Coefficients of expansion of space charge density are defined by inverse Fourier transformation:

$$Q_{mnl}^{(c)} = \frac{8}{N_x N_y N_z} \sum_{i=1}^{N_x-1} \sum_{j=1}^{N_y-1} \sum_{k=0}^{N_z-1} Q_{ijk} \sin\left(\frac{\pi ni}{N_x}\right) \sin\left(\frac{\pi mj}{N_y}\right) \cos\left(\frac{2\pi kl}{N_z}\right),$$ (7.56)

$$Q_{mnl}^{(s)} = \frac{8}{N_x N_y N_z} \sum_{i=1}^{N_x-1} \sum_{j=1}^{N_y-1} \sum_{k=1}^{N_z-1} Q_{ijk} \sin\left(\frac{\pi ni}{N_x}\right) \sin\left(\frac{\pi mj}{N_y}\right) \sin\left(\frac{2\pi kl}{N_z}\right),$$ (7.57)

with analogous expressions for potential expansion. After substitution of Fourier expansion (7.54), (7.55) into Poisson's equation (7.52), coefficients of space charge and potential expansion are connected by algebraic relationship:

$$\overline{U}_{mnl}^{(c,s)} = \frac{\overline{Q}_{mnl}^{(c,s)}}{\left(\frac{\pi n}{a}\right)^2 + \left(\frac{\pi m}{b}\right)^2 + \left(\frac{2\pi l}{L}\right)^2}.$$ (7.58)

After calculation of coefficients, Eq.(7.58), the potential is found as Fourier series (7.54).

Electrostatic field at the point of every macroparticle is found via numerical differentiation of polynomial [26]:

$$\vec{E} = - \text{ grad } \widetilde{U}\,(\widetilde{x},\,\widetilde{y},\,\widetilde{z}),$$ (7.59)

$$\widetilde{U}\,(\widetilde{x},\,\widetilde{y},\,\widetilde{z}) = a_1\widetilde{x} + a_2\widetilde{y} + a_3\widetilde{z} + a_4\widetilde{x}^2 + a_5\widetilde{y}^2 + a_6\widetilde{z}^2 + a_7\widetilde{x}\widetilde{y} + a_8\widetilde{x}\widetilde{z} + a_9\widetilde{y}\widetilde{z},$$ (7.60)

$$\widetilde{x} = \frac{x - x_i}{h_x}, \qquad \widetilde{y} = \frac{y - y_j}{h_y}, \qquad \widetilde{z} = \frac{z - z_k}{h_z}.$$ (7.61)

The polynomial, Eq. (7.60), describes potential in the vicinity of each macroparticle. It is a continuous function of coordinates, which provides "local smoothing" of discrete potential function, U_{ikj}, defined at grid nodes. Differentiation of Eq. (7.60) also gives continuous function of coordinates, which is more smoothed than piece-linear function obtained from commonly used finite-difference method. Differentiation with local smoothing is especially usefull for 3D space charge problem with limited number of macroparticles and grid nodes.

To provide differentiation of potential, the 27 nearest nodes to each particle are selected with the closest node (i, j, k). Deviation of the polynomial, Eq. (7.60), from grid values of potential, is minimized in selected 27 nodes:

$$\sum_{n=i-1}^{i+1} \sum_{m=j-1}^{j+1} \sum_{l=k-1}^{k+1} [\widetilde{U}\,(\widetilde{x}_n,\,\widetilde{y}_m,\,\widetilde{z}_l) - U_{n,\,m,\,l}]^2 = \min$$ (7.62)

From Eq. (7.62), the coefficients a_i, i=1,..9 are [26]:

$$a_1 = \frac{\partial \widetilde{U}}{\partial \widetilde{x}}\,(0,\,0,\,0) = \frac{1}{9} \sum_{m=j-1}^{j+1} \sum_{l=k-1}^{k+1} \frac{1}{2}\,(U_{i+1,\,m,\,l} - U_{i-1,\,m,\,l}),$$ (7.63a)

$$a_2 = \frac{\partial \widetilde{U}}{\partial \widetilde{y}}(0, 0, 0) = \frac{1}{9} \sum_{n=i-1}^{i+1} \sum_{l=k-1}^{k+1} \frac{1}{2} (U_{n, j+1, \; l} - U_{n, j-1, \; l}) , \qquad (7.63b)$$

$$a_3 = \frac{\partial \widetilde{U}}{\partial \widetilde{z}}(0, 0, 0) = \frac{1}{9} \sum_{n=i-1}^{i+1} \sum_{m=j-1}^{j+1} \frac{1}{2} (U_{n, m, k+1} - U_{n, m, k-1}) , \qquad (7.63c)$$

$$2a_4 = \frac{\partial^2 \widetilde{U}}{\partial \widetilde{x}^2}(0, 0, 0) = \frac{1}{9} \sum_{m=j-1}^{j+1} \sum_{l=k-1}^{k+1} (U_{i+1, m, \; l} - 2U_{i, m, \; l} + U_{i-1, m, \; l}), \qquad (7.63d)$$

$$2a_5 = \frac{\partial^2 \widetilde{U}}{\partial \widetilde{y}^2}(0, 0, 0) = \frac{1}{9} \sum_{n=i-1}^{i+1} \sum_{l=k-1}^{k+1} (U_{n, j+1, \; l} - 2U_{n, j, \; l} + U_{n, j-1, \; l}) , \qquad (7.63e)$$

$$2a_6 = \frac{\partial^2 \widetilde{U}}{\partial \widetilde{z}^2}(0, 0, 0) = \frac{1}{9} \sum_{n=i-1}^{i+1} \sum_{m=j-1}^{j+1} (U_{n, m, k+1} - 2U_{n, m, k} + U_{n, m, k-1}) , \qquad (7.63f)$$

$$a_7 = \frac{\partial^2 \widetilde{U}}{\partial \widetilde{x} \partial \widetilde{y}}(0, 0, 0) = \frac{1}{3} \sum_{l=k-1}^{k+1} \frac{1}{4} (U_{i+1, j+1, \; l} - U_{i+1, j-1, \; l} - U_{i-1, j+1, \; l} + U_{i-1, j-1, \; l}) , \qquad (7.63g)$$

$$a_8 = \frac{\partial^2 \widetilde{U}}{\partial \widetilde{x} \partial \widetilde{z}}(0, 0, 0) = \frac{1}{3} \sum_{m=j-1}^{j+1} \frac{1}{4} (U_{i+1, m, k+1} - U_{i+1, m, k-1} - U_{i-1, m, k+1} + U_{i-1, m, k-1}) , \qquad (7.63h)$$

$$a_9 = \frac{\partial^2 \widetilde{U}}{\partial \widetilde{y} \partial \widetilde{z}}(0, 0, 0) = \frac{1}{3} \sum_{n=i-1}^{j+1} \frac{1}{4} (U_{n, j+1, k+1} - U_{n, j+1, k-1} - U_{n, j-1, k+1} + U_{n, j-1, k-1}) . \qquad (7.63i)$$

Components of electric field are:

$$E_x = - (a_1 + 2a_4 \widetilde{x} + a_7 \widetilde{y} + a_8 \widetilde{z}) \frac{1}{h_x} , \qquad (7.64a)$$

$$E_y = - (a_2 + 2a_5 \widetilde{y} + a_7 \widetilde{x} + a_9 \widetilde{z}) \frac{1}{h_y} , \qquad (7.64b)$$

$$E_z = - (a_3 + 2a_6 \widetilde{z} + a_8 \widetilde{x} + a_9 \widetilde{y}) \frac{1}{h_z} . \qquad (7.64c)$$

In Table 6 results of space charge field calculation of Gaussian bunch with distribution, Eq. (7.48), are presented. Error δ, Eq. (7.51), is within the interval of $(1.5 - 5) \cdot 10^{-2}$. In contrast with Table 5, errors are not very sensitive to grid size and number of particles. It is a result of smoothing

of potential grid function utilizing polynomial, Eq. (7.60). Computing time, required for 3D space charge simulations on Alpha Server 2100 5/250 computer (250 MHz CPU) is

$$t = (1.3 \cdot N_g + 3 \cdot N) \cdot 10^{-5} \text{ sec,} \tag{7.65}$$

where $N_g = \frac{1}{2} N_x \cdot N_y \cdot N_z$ is a number of grid points. Required computing time is a linear function of number of grid points, N_g, and number of macroparticles, N, which is typical for fast methods of space charge calculations [11]. The same dependencies are valid for 2D Poisson's solvers in Cartesian and cylindrical coordinates.

7.6 Space charge solver for 2D relativistic beam with large energy spread

Considered Poisson's solvers are used for a beam with small energy spread $\Delta\gamma/\gamma \ll 1$. In many applications, including beam bunching in klystrons and RF photo-injectors, it is required to simulate dynamics of a relativistic beam with large energy spread $\Delta\gamma/\gamma \sim 1$. This is achieved via simulation of particle-particle interaction utilizing Green function method.

Field created by a relativistic ring (see Fig. 12) with charge density ρ, length h, internal radius r_1, external radius r_2, propagating in an ideally conducted pipe of radius a with longitudinal velocity v_s and energy γ_s is given by [27] :

$$E_z = \frac{\rho}{\gamma_s \, \varepsilon_o} \sum_{n=1}^{N} \frac{J_o(v_n \frac{r}{a})}{v_n^2 \, J_1^2(v_n)} f(r_1, r_2) \cdot \left\{ \begin{array}{l} F_1 \cdot \text{sgn}(z - z_s), \ |z - z_s| \geq h/2 \\ F_2 \cdot \text{sgn}(z - z_s), \ |z - z_s| < h/2 \end{array} \right., \tag{7.66}$$

$$E_r = \frac{\rho}{\varepsilon_o} \sum_{n=1}^{N} \frac{J_1(v_n \frac{r}{a})}{v_n^2 \, J_1^2(v_n)} f(r_1, r_2) \cdot \left\{ \begin{array}{l} F_1, \ |z - z_s| \geq h/2 \\ F_3, \ |z - z_s| < h/2 \end{array} \right., \tag{7.77}$$

$$B_\theta = \frac{v_s}{c^2} E_r, \tag{7.78}$$

where

$$F_1 = [\exp(v_n \gamma_s \frac{h}{2a}) - \exp(-v_n \gamma_s \frac{h}{2a})] \exp(-v_n \gamma_s \frac{|z - z_s|}{a}), \tag{7.79}$$

$$F_2 = [\exp(v_n \gamma_s \frac{|z - z_s|}{a}) - \exp(-v_n \gamma_s \frac{|z - z_s|}{a})] \cdot \exp(-v_n \gamma_s \frac{h}{2a}), \tag{7.80}$$

$$F_3 = 2 - [\exp(-v_n \gamma_s \frac{|z - z_s|}{a}) + \exp(v_n \gamma_s \frac{|z - z_s|}{a})] \cdot \exp(-v_n \gamma_s \frac{h}{2a}), \tag{7.81}$$

$$f(r_1, r_2) = r_2 \cdot J_1(v_n \frac{r_2}{a}) - r_1 \cdot J_1(v_n \frac{r_1}{a}). \tag{7.82}$$

Space charge field acting at every particle is calculated as superposition of fields created by all other particles. This method is much slower than Poisson's solvers described above, because it requires number of operations proportional to square of number of particles.

8 CHOICE OF MODELING PARAMETERS AND TEST PROBLEMS FOR CODE VALIDATION

Particle-in-cell models are characterized by large number of parameters, which are defined by compromise between required accuracy and required computing time and memory. Spatial and time discretization of the self-consistent problem affects stability of numerical solutions. Combination of model parameters (integration step τ, number of macroparticles N and number of grid points N_g.) has to provide the most comprehensive and accurate description of the modeling system using the optimal resources of computer.

For adequate simulations, the size of macroparticle, δr, has to be larger than average distance between particles Δr and smaller than characteristic distance, D, where variation of space charge density is significant. In present model, particle sizes are equal to mesh sizes h_x, h_y, h_z, h_r. If particle size is too large, $\delta r \approx D$, charge distribution in model becomes too smooth. It results in loosing of effects connected with specific space charge distribution. On the contrary, with $\delta r < \Delta r$, unphysical variation of space charge density appears and particle-particle collisions are overestimated in the model.

Good tests for correct choice of model parameters give calculation of processes, which have analytical solutions. It is a necessary stage of the project to check the program and to verify the optimal choice of model parameters.

8.1. Drift of uniform beam in free space

Spread of round uniform beam in free space is described by KV equation for beam envelope R [18]:

$$\frac{d^2R}{dz^2} - \frac{\ni^2}{R^3} - \frac{2\,I}{R\,(\beta\gamma)^3 I_c} = 0 \,.\qquad(8.1)$$

For space charge dominated beam with negligible emittance, $\ni \approx 0$ and $R_o^{'} = 0$, Eq. (8.1) has an approximate solution:

$$\frac{R}{R_o} = 1 + 0.25\,Z^2 - 0.017\,Z^3, \qquad Z = \frac{z}{R_o}\sqrt{\frac{4\,I}{I_c\,\beta^3\,\gamma^3}}\,,\qquad(8.2)$$

where R_o is an initial radius of the beam. In Fig. 13 results of evolution of envelope of the 150 keV, 1 A proton beam are presented. Deviation of numerically calculated beam envelope from

solution of Eq. (8.1) is less than 10^{-4}. Simulation utilizing 10^4 particles on the grid N_x x N_y = 256 x 256 with 360 integration steps takes 167 sec (here and below the CPU time is given for Alpha Server 2100 5/250, 250 MHz CPU).

8.2 Drift of Gaussian beam in free space

If beam is not uniform, its density profile as well as beam sizes are changed in drift space. Evolution of Gaussian beam with zero emittance in drift space under self non-linear space charge forces is described by the expression [28]:

$$\rho\,(r) = \frac{\rho_o \exp{(-2\,\xi_o^2)}}{a_o + a_1 F + a_2 F^2 + a_3 F^3 + a_4 F^4 + a_5 F^5 + a_6 F^6}\,, \qquad (8.3)$$

where the following notations are used:

$$\xi_o = \frac{r_o}{R_o}, \quad F = \sqrt{\frac{1 - \exp{(-2\xi_o^2)}}{\xi_o^2}}\,, \quad \eta = \frac{4\,I}{I_c\,\beta^3\,\gamma^3}\,\frac{z^2}{R_o^2}\,, \qquad (8.4a)$$

$$r = r_o\,(1 + \frac{1}{4}\,\eta\,F^2 - 0.017\,\eta^{3/2}\,F^3)\,, \qquad (8.4b)$$

$$a_o = 1 + \eta\,\exp{(-2\xi_o^2)}, \quad a_1 = -\,0.102\,\eta^{3/2}\,\exp{(-2\xi_o^2)}\,, \qquad (8.4c)$$

$$a_2 = \frac{1}{4}\,\eta^2\,\exp{(-2\xi_o^2)}, \qquad (8.4d)$$

$$a_3 = 0.017\,\eta^{3/2} - 0.0425\,\eta^{5/2}\,\exp{(-2\xi_o^2)}\,, \qquad (8.4e)$$

$$a_4 = 1.734 \cdot 10^{-3}\,\eta^3 \exp(-2\xi_o^2) - \frac{1}{16}\,\eta^2\,, \qquad (8.4f)$$

$$a_5 = 0.01275\,\eta^{5/2}, \quad a_6 = -\,5.78 \cdot 10^{-4}\,\eta^3\,. \qquad (8.4g)$$

Formula (8.3) predicts uniforming of the Gaussian beam at the distance where parameter $\eta = 3.8$. In Fig. 14 results of evolution of 35 MeV, 4.7 A, D$^+$ beam with initial Gaussian distribution and initial radius of R_o = 1.3 cm are presented. Simulation with 10^4 particles on the grid 256 x 256 with 1200 integration steps takes 7.5 min. Numerical results indicate good agreement with theory.

8.3. Beam equilibrium with space charge

Beam distribution function $f\,(x, y,\,p_x,\,p_y)$ is conserved in time-independent focusing field, if beam is in equilibrium with external field. Stationary self-consistent beam distribution function is a solution of Vlasov-Poisson's equations:

$$\frac{1}{m\gamma}\left(\frac{\partial f}{\partial x}\,p_x + \frac{\partial f}{\partial y}\,p_y\right) - q\left(\frac{\partial f}{\partial p_x}\,\frac{\partial V}{\partial x} + \frac{\partial f}{\partial p_y}\,\frac{\partial V}{\partial y}\right) = 0 ,$$

$$\tag{8.5}$$

$$\frac{1}{r}\frac{\partial}{\partial r}\left(r\,\frac{\partial U_b}{\partial r}\right) = -\frac{q}{\varepsilon_o}\int_{-\infty}^{\infty}\int_{-\infty}^{\infty} f\,(x,p_x,y,p_y)\,dp_x\,dp_y,$$

where $V = U_b + \gamma^{-2}U_{ext}$ is a total potential of the structure and U_{ext} is an external focusing potential. General treatment of the problem (8.5) for arbitrary distribution function was given in [29]. In Table 7 self-consistent solutions for different beam distributions are presented.

Fig. 15 illustrates equilibrium of a 150 keV, 0.5 Amp, 0.07 π cm mrad proton beam with distribution function

$$f = f_o \exp\left(-2\,\frac{p_x^2 + p_y^2}{(\varepsilon/R)^2} - \frac{(x^2+y^2)^2}{R^4}\right) ,$$

$$\tag{8.6}$$

which propagates in focusing field

$$E(r) = -\frac{mc^2}{q\,R\gamma}\left[\left(\frac{\varepsilon}{R}\right)^2\left(\frac{r^3}{R^3}\right) + \frac{2I}{I_c\,\beta\gamma}\left(\frac{R}{r}\right)\mathrm{erf}\left(\frac{r^2}{R^2}\right)\right].$$

$$\tag{8.7}$$

The ratio of space-charge-depressed tune shift to undepressed one is $\nu/\nu_o = 0.05$. Simulation confirms that beam distribution remains constant, while particles perform nonlinear oscillations within the beam. Conservation of beam distribution indicates equilibrium condition. Simulations with $3\cdot10^4$ particles on the grid $N_x \times N_y = 512 \times 512$ with 6500 integration steps takes 163 min.

8.4. Drift of 3D uniformly charged ellipsoid in free space

Up to now we have considered 2D tests for transverse space charge forces. Fully 3D test is available utilizing dynamics of uniformly populated ellipsoid. It is well known that there is no distribution function in six-dimensional phase space, which leads to a solution of the self-consistent problem as a uniformly charged 3D ellipsoid in real space. However, self-consistent solution is valid for a 3D time-dependent ellipsoid with zero phase-space volume [30]. In a free space, evolution of ellipsoid boundaries, R_x, R_y, R_z, is described by 3D equations:

$$\frac{d^2R_x}{dz^2} = 3\,r_o\,\frac{Q_e}{q\bar\beta_z^2}\,\frac{M_x(R_x, R_y, R_z)}{R_y\,R_z},$$

$$\tag{8.8}$$

$$\frac{d^2R_y}{dz^2} = 3\,r_o\,\frac{Q_e}{q\bar\beta_z^2}\,\frac{M_y(R_x, R_y, R_z)}{R_x\,R_z},$$

$$\tag{8.9}$$

$$\frac{d^2R_z}{dz^2} = 3\,r_o\,\frac{Q_e}{q\bar\beta_z^2}\,\frac{M_z(R_x, R_y, R_z)}{R_x\,R_y}.$$

$$\tag{8.10}$$

where Q_e is the charge of ellipsoid, r_o is the classical radius of particles, and M_x, M_y, M_z are defined by the expressions:

$$M_x(R_x, R_y, R_z) = \frac{1}{2} \int_o^\infty \frac{R_x R_y R_z \, ds}{(R_x^2 + s) \sqrt{(R_x^2 + s)(R_y^2 + s)(R_z^2 + s)}} \, , \qquad (8.11)$$

$$M_y(R_x, R_y, R_z) = \frac{1}{2} \int_o^\infty \frac{R_x R_y R_z \, ds}{(R_y^2 + s) \sqrt{(R_x^2 + s)(R_y^2 + s)(R_z^2 + s)}} \, , \qquad (8.12)$$

$$M_z(R_x, R_y, R_z) = \frac{1}{2} \int_o^\infty \frac{R_x R_y R_z \, ds}{(R_z^2 + s) \sqrt{(R_x^2 + s)(R_y^2 + s)(R_z^2 + s)}} \, . \qquad (8.13)$$

In Figs. 16, 17 numerical results of drift of proton ellipsoid with $Q_e = 3$ nK, initial values of semi-axes $R_x = 2$ cm, $R_y = 1$ cm, $R_z = 4$ cm, and longitudinal velocity of $\beta_z = 0.01$ are presented. Calculations utilizing $2 \cdot 10^4$ particles on the grid $\frac{1}{2} N_x \times N_y \times N_z = 64 \times 128 \times 512$ with 200 integration steps took 158 min. Difference in analytical and numerical values of ellipsoid sizes are within the limit of 3%.

8.5. Beam bunching

One-dimensional problem of beam bunching with space charge has an approximate analytical solution [31]. Consider non relativistic beam of particles with energy qU_o and radius R propagating in a tube of radius a. Injected beam passes through the gap of length d with applied voltage of $U(t) = U_1 \cdot \sin\omega t$. Particle bunching in drift space is characterized by the value of first harmonic of induced current I_1 as a function of bunching parameter X

$$\frac{I_1}{I} = 2 \, J_1 \, (X) \, , \qquad X = (\frac{U_1 \, M_1}{2 \, U_o}) \, (\frac{\omega_o \, z}{v}) \, [\frac{\sin (\frac{\omega_q \, z}{v})}{(\frac{\omega_q \, z}{v})}] \, , \qquad (8.22)$$

where $J_1 \, (X)$ is the Bessel function, M_1 is the coupling coefficient of the beam with modulation gap:

$$M_1 = \frac{\sin (\theta/2)}{\theta/2} \, , \qquad (8.23)$$

$\theta = \omega d/v$ is the transit time angle through the gap, $\omega_q = \sqrt{F_p} \, \omega_p$ is the reduced plasma frequency of the beam, $\omega_p = 2 \, (c/R) \sqrt{I / (\beta I_c)}$ is the plasma frequency for an unbounded beam and F_p is the form factor of reduction of plasma frequency due to finite radius of the beam and tube:

$$F_p = 2.56 \ \frac{J_1^2 \ (2.4 \ \frac{R}{a})}{1 + \dfrac{5.76}{(\omega R \ /v)^2}} \ . \tag{8.24}$$

Numerical value of the first harmonic of bunched beam is calculated as follow:

$$\frac{I_1(z)}{I} = \frac{2}{N} \ \sqrt{[\sum_{n=1}^{N} \ \cos \omega t_n(z)]^2 + [\sum_{n=1}^{N} \ \sin \omega t_n(z)]^2} \ , \tag{8.25}$$

where $t_n(z)$ is the time when the n-th particle reaches the point z. Numerical example of bunching of 150 keV, 1 A, R/a = 0.8 proton beam is given in Fig. 18. Simulations with $5 \cdot 10^3$ particles on the $N_r \times N_z = 256 \times 256$ grid with 4000 steps takes 13 min.

9 EXAMPLES OF BEAM DYNAMICS SIMULATION WITH SPACE CHARGE

9.1. Low energy beam transport

Beam quality in accelerator essentially depends on injection part. Many low-energy beam transport system employ axial-symmetric lenses (both electrostatic and magnetostatic). Such lenses are characterized by high values of spherical aberrations, which results in over-focusing of particles with radius. Effect of emittance growth due to spherical aberrations is estimated as [32]:

$$\frac{\ni}{\ni_o} = 1 + K \ \delta^2, \tag{9.1}$$

$$\delta = \frac{C_s \ R^4}{\ni \ f^4} \ , \tag{9.2}$$

where C_s is the spherical aberration coefficient, f is the focal length of the lens and parameter K=0.1...0.5 depends on beam distribution. Another source of beam emittance distortion is nonlinear space charge field of the beam. Emittance growth in drift space between lenses due to nonlinear space charge of the beam is estimated by the same Eq. (9.1) with K $\approx$ 0.014and parameter δ [32]

$$\delta = 4 \ \frac{z}{\ni} \ \frac{I}{I_c \ \beta^3 \ \gamma^3} \ . \tag{9.3}$$

In Figs. 19, 20, 21 results of 50 keV, 20 mA, 0.075 π mm mrad proton beam dynamics in transport line [33] are presented. Low Energy Beam Transport line (LEBT) consists of two axial-symmetric magnetic lenses with longitudinal field distribution presented in Fig. 19a. Magnetic field of the LEBT was interpolated on the grid $N_z \times N_r = 432 \times 15$. Beam simulations with $N = 10^4$ particles on the grid $N_x \times N_y = 256 \times 256$ with 7540 integration steps takes 60 min. Simulations

clearly indicate beam redistribution in phase space due to nonlinear space charge forces and lens aberrations.

9.2. Effect of random errors in RFQ electrodes on beam transmission efficiency

Most of low energy ion injector lines are equipped with RFQ linacs, which allow to accelerate high current beams. RIKEN heavy ion injector employs frequency tunable RFQ [34]. Random errors in manufacturing of RFQ vane tips result in amplitude growth of transverse and longitudinal oscillations. To obtain accurate estimation of this effect on beam dynamics, simulations were performed with the following parameters randomly distributed at every cell within the maximum error of $\pm \Delta$: cell lengths L_i, aperture radius a_i, maximum distance from axis to electrodes ma_i, and axis displacement δr_{oi}. Results of simulation of 1 mA Ar^{+8} beam dynamics are presented in Fig. 22. In Table 8 comparison is done for beam transmission efficiency N_f / N_o, and for the ratio of final and initial transverse phase space densities of the beam

$$ \frac{j_f}{j_o} = \frac{N_f / \varepsilon_f}{N_o / \varepsilon_o} , \tag{9.4} $$

where N_o is the initial number of particles and N_f is the number of accelerated particles. Simulations with $N_o = 5000$ and 1600 integration steps takes 2 min without space charge forces and 140 min with space charge forces on the grid $\frac{1}{2}N_x \times N_y \times N_z = 32 \times 64 \times 256$.

Random errors in the RFQ geometry induce particle losses in longitudinal and transverse directions. Transverse losses are defined as a fraction of particles which are stopped during simulations due to reaching boundary of the channel. Longitudinal particle losses are defined as a fraction of particles which are behind the accelerated bunch. From the results of simulations it follows that the error of 50 microns does not create any serious degradation of the beam parameters while an error of 100 microns could cause notable decreasing of beam transmission efficiency and reduction of phase space density. During machinery, the engineering tolerance of 50 microns was adopted for vane tips fabrications. Operation of RIKEN RFQ linac indicates that 90% of transmission efficiency is obtained steadily [34].

CONCLUSIONS

Software for beam dynamics study with space charge in 2D and 3D geometry is developed. Program BEAMPATH covers most of the problems for intense beam simulations in linear accelerators and beamlines. Developed algorithms provide high accuracy with reasonable consuming of computer time. Given numerical examples demonstrate efficiency of calculations.

REFERENCES

1. B.Austin, T.W.Edwards, J.E.O'Meara, M.L.Palmer, D.A.Swenson and D.E.Young, MURA report No. 713, 1965; D.A.Swenson and J.Stovall, LANL internal report MP-3-19, 1968; J.P.Boicourt, AIP Conference Proceedings 177, Editor Charles R.Eminhizer, New York, 1988, p.1.

2. K.R.Crandall and T.P.Wangler, AIP Conference Proceedings 177, Editor Charles R.Eminhizer, New York, 1988, p.22.

3. A.Friedman, D.P.Grote, I.Haber, Phys. Fluids B: Plasma Physics 4, (1992), p. 2203.

4. S.Machida, Nuclear Instruments and Methods, A 309 (1991), p.43.

5. F.W.Jones, G.H.Mackenzie and H.Schonauer, Particle Accelerators 31, (1990), p.199.

6. A.U.Luccio, J.Beebe-Wang, M.Blaskiewicz, J.Galambos, J.Holmes and D.Olsen, AIP Conference Proceedings 448, Editors A.U.Luccio and W.T.Weng, New York, 1998, p.390.

7. J.Galambos, S.Danilov, D.Jeon, J.Holmes, D.Olsen, J.Beebe-Wang, A.Luccio, Proceedings of the 1999 Particle Accelerator Conference, New York, 1999, Editors A.Luccio, W.MacKay, p. 3143.

8. C.R.Prior, AIP Conference Proceedings 448, Editors A.U.Luccio and W.T.Weng, New York, 1998, p.85.

9. D.L.Bruhwiler and N.F.Reusch, AIP Conference Proceedings 297, New York, 1993, p.524

10. Y.K.Batygin, Proceedings of the 3rd European Particle Accelerator Conference (EPAC92), Berlin, Germany, 24-28 March, 1992, Editors: H.Henke, H.Homeyer and Ch. Petit-Jean-Genaz, Editions Frontiers ISBN 2-86332-114-5, p. 822 (1992); Y.K.Batygin, AIP Conference Proceedings 297, p.p.196-202, p.p. 419 - 426, Los Alamos, (1994); Y.K.Batygin, Accelerators, Vol. 20, Moscow, Energoizdat, (1981), p.p. 52-55 (in Russian).

11. R.W.Hockney and J.W.Eastwood, Computer simulation using particles, McGraw-Hill, 1981.

12. H.Yoshida, Celestial Mechanics and Dynamical Astronomy 56, 1993, p. 27.

13. R.D.Ruth, IEEE Trans. Nucl. Sci. NS-30, 1983, p. 2669.

14. D.Potter, Computational Physics, John Wiley &Sons Ltd., 1973.

15. V.Bargmann, L.Michel, V.L.Telegdi, Phys. Rev. Lett. 2 (1959) 435.

16. Y.Batygin and T.Katayama, Physical Review E, Vol. 58, (1998), 1019.

17. J.Struckmeier, J.Klabunde and M.Reiser, Particle Accelerators, 15, 1984, p. 47.

18. I.M.Kapchinsky, Theory of Resonance Linear Accelerators, Harwood, 1985.

19. G.E.Forsythe, M.A.Malcolm and C.B.Moler, Computer Methods for Mathematical Computations, Printece-Hall, N.J., 1977.

20. K.L.Brown, R.V.Servranckx, AIP Conference Proceedings 127, Ed. M.Month, P.Dahl, M.Dienes, New York, 1985, p. 64.

21. K.L.Brown, F.Rothacker, D.C.Carey and Ch.Iselin, Report SLAC-91, 1974.

22. V.Lebedev, V.Parchomchuk, V.Shiltsev and G.Stupakov, Part. Accel. 44, 147 (1994).

23. J.D.Lawson, The Physics of Charged-Particle Beams, Clarendon Press, Oxford, 1977.

24. W.H.Press, B.P.Flannery, S.A.Teukolsky, W.T.Vetterling, Numerical Recipes The Art of Scientific Computing, Cambridge University Press, 1986.

25. K.Takayama, Lettere al Nuovo Cimento, Vol. 34, No.7, p.190 (1982).

26. A.S.Roshal, Simulation of charged-particle beams, Moscow, Atomizdat, 1979 (in Russian).

27. W.R.Smythe, Static and Dynamic Electricity, 3rd edition, McGra-Hill, New York, 1969.

28. D.L.Bruhwiler and Y.K.Batygin, Proceedings of the PAC95, Dallas, p. 3254 (1995).

29. Y. K.Batygin, Phys. Review E, 53, p. 5358, (1996).

30. Y.K.Batygin, Physics of Plasmas, Vol. 8, No. 6, p. 3103 (2001).

31. Yu.A.Katsman, Microwave Devices, Moscow, 1973 (in Russian).

32. Y.Batygin, A.Goto and Y.Yano, Proceedings of the 5th European Particle Accelerator Conference (EPAC96), Barcelona, Spain, Ed. by S.Myers, A.Pacheco, R.Pascual. Ch. Petit-Lean-Genaz, J.Poole, Institute of Physics Publishing, Bristol and Philadelphia, 1996, p. 2497.

33. S.Fujimura and A.Ueno, Proceedings of the XVIII International Linear Accelerator Conference (LINAC96), Ed. C.Hill, M.Vretenar, CERN, (1996), p.343.

34. O.Kamigaito, A.Goto, Y.Miyazawa, T.Chiba, M.Hemmi, S.Kohara, M.Kase, Y.Batygin, Y.Yano, Proceedings of the 5th European Particle Accelerator Conference (EPAC96), Barcelona, Spain, Ed. by S.Myers, A.Pacheco, R.Pascual, Ch. Petit-Lean-Genaz, J.Poole, Institute of Physics Publishing, Bristol and Philadelphia, 1996, p.786.

Table 1. Characteristics of the BEAMPATH code

Types of beam symmetry for space charge calculation:

        z - uniform beam

        - axial symmetric beam

        - quadrupole symmetric beam

Accelerating and focusing elements

        - arbitrary order multipole lenses

        - axial-symmetric magnetic lenses (solenoids, permanent magnets)

        - RF gaps and cavities

        - radio frequency quadrupoles (RFQ)

        - bending magnets

        - accelerating waveguides

        - user defined element

Typical CPU running time (for Alpha Server 2100 5/250 computer, 250 MHz CPU)

Without space charge, 2D interpolation of external field on the grid $N_r \times N_z = 15 \times 432$	$10^{-5} \dfrac{\text{second}}{\text{particle step}}$
Space charge problem: On 2D grid $N_x \times N_y = 256 \times 265$	$4 \cdot 10^{-5} \dfrac{\text{second}}{\text{particle step}}$
On 2D grid $N_x \times N_y = 512 \times 512$	$5 \cdot 10^{-5} \dfrac{\text{second}}{\text{particle step}}$
On 3D grid $\frac{1}{2}N_x \times N_y \times N_z = 32 \times 64 \times 128$	$10^{-3} \dfrac{\text{second}}{\text{particle step}}$
On 3D grid $\frac{1}{2}N_x \times N_y \times N_z = 128 \times 256 \times 128$	$10^{-2} \dfrac{\text{second}}{\text{particle step}}$

Table 2. Characteristics of different phase space distributions, $\rho^2 = (\frac{x}{a_x})^2 + (\frac{y}{a_y})^2$.

	KV	"Water bag"	Parabolic	Gaussian
Definition	$\dfrac{1}{2\pi F_o}(F - F_o)$	$\dfrac{2}{\pi^2 F_o^2}, F \le F_o$	$\dfrac{6}{\pi^2 F_o^2}(1 - \dfrac{F}{F_o})$	$\dfrac{1}{\pi^2 F_o^2}\exp(-\dfrac{F}{F_o})$
Rms emittance x	F_o	$\dfrac{2}{3}F_o$	$\dfrac{F_o}{2}$	$2 F_o$
Rms emittance y	F_o	$\dfrac{2}{3}F_o$	$\dfrac{F_o}{2}$	$2 F_o$
Projection $\dfrac{F_o\, a_x a_y}{\sqrt{\ }}$ (x,y)	$1, \rho^2 \le 1$	$2(1 - \dfrac{\rho^2}{F_o})$	$3(1 - \dfrac{\rho^2}{F_o})^2$	$\exp(-\dfrac{\rho^2}{F_o})$
Projection πF_o (x, x')	$1, \rho_x^2 \le F_o$	$2(1 - \dfrac{\rho_x^2}{F_o})$	$3(1 - \dfrac{\rho_x^2}{F_o})^2$	$\exp(-\dfrac{\rho_x^2}{F_o})$
Projection πF_o (y, y')	$1, \rho_y^2 \le F_o$	$2(1 - \dfrac{\rho_y^2}{F_o})$	$3(1 - \dfrac{\rho_y^2}{F_o})^2$	$\exp(-\dfrac{\rho_y^2}{F_o})$
Equation F=F(G)	$F = F_o$	$F = F_o\sqrt{G}$	$2F^3 - 3F_o F^2 + GF_o^3 = 0$	$(1-G)-(1+\dfrac{F}{F_o})\cdot\exp(-\dfrac{F}{F_o})=0$

Table 3. Error $= \left| \dfrac{\text{numerical} - }{} \right|$ of generation of rms beam emittance

Distribution	Number of particles, N		
	10^3	10^4	10^5
KV	$1 \cdot 10^{-2}$	$5 \cdot 10^{-3}$	$6 \cdot 10^{-4}$
"Water Bag"	$9 \cdot 10^{-3}$	$5 \cdot 10^{-3}$	$5 \cdot 10^{-4}$
Parabolic	$2 \cdot 10^{-2}$	$7 \cdot 10^{-3}$	$1 \cdot 10^{-3}$
Gaussian	$3 \cdot 10^{-2}$	$7 \cdot 10^{-3}$	$3 \cdot 10^{-3}$

Table 4. Error of Gauss theorem, , and required time, t, sec (Alpha Server 2100 5/250) for 2D test problem with random initial data.

Grid N_x x N_y	t	
16 x 16	$1. \cdot 10^{-3}$	$1.9 \cdot 10^{-2}$
32 x 32	$3.3 \cdot 10^{-3}$	$1.01 \cdot 10^{-2}$
64 x 64	$1.2 \cdot 10^{-2}$	$5.3 \cdot 10^{-3}$
128 x 128	$4.7 \cdot 10^{-2}$	$2.7 \cdot 10^{-3}$

Table 5. Error in calculation of the field of Gaussian bunch in 2D cylindrical coordinates.

Grid N_r x N_z	Number of particles		
	$5 \cdot 10^3$	$5 \cdot 10^4$	$5 \cdot 10^5$
32 x 32	$7.6 \cdot 10^{-2}$	$7.4 \cdot 10^{-2}$	$7.3 \cdot 10^{-2}$
64 x 64	$2.9 \cdot 10^{-2}$	$2.6 \cdot 10^{-2}$	$2.5 \cdot 10^{-2}$
128 x 128	$1.9 \cdot 10^{-2}$	$1.3 \cdot 10^{-2}$	$1 \cdot 10^{-2}$

Table 6. Error   and time t, sec (Alpha Server 2100 5/250) for space charge calculation of Gaussian bunch in 3D Cartesian coordinates.

$\frac{N_x}{2}{\cdot}N_y{\cdot}N_z$	Number of macroparticles, N					
Grid	$5{\cdot}10^3$		$5{\cdot}10^4$		$5{\cdot}10^5$	
		t		t		t
16·32·64	$4.8{\cdot}10^{-2}$	0.5	$3.5{\cdot}10^{-2}$	1.6	$3.5{\cdot}10^{-2}$	12.0
16·32·128	$4.7{\cdot}10^{-2}$	0.9	$3.2{\cdot}10^{-2}$	2.3	$3.2{\cdot}10^{-2}$	16.0
32·64·64	$3.7{\cdot}10^{-2}$	1.6	$2.1{\cdot}10^{-2}$	3.1	$2.0{\cdot}10^{-2}$	16.0
32·64·128	$3.7{\cdot}10^{-2}$	3.2	$1.9{\cdot}10^{-2}$	4.7	$1.8{\cdot}10^{-2}$	20.8
32·64·256	$3.8{\cdot}10^{-2}$	6.5	$2.0{\cdot}10^{-2}$	8.7	$1.8{\cdot}10^{-2}$	30.5
64·128·128	$3.9{\cdot}10^{-2}$	13.5	$1.9{\cdot}10^{-2}$	15.9	$1.6{\cdot}10^{-2}$	37.0
64·128 ·256	$4.2{\cdot}10^{-2}$	28	$2.0{\cdot}10^{-2}$	30.6	$1.6{\cdot}10^{-2}$	58.0

Table 7. Self-consistent beam equilibrium with space charge (ε-normalized beam emittance, R- beam radius).

Distribution function	Definition	Required focusing field
KV	$f = f_o \; \delta(\dfrac{p_x^2 + p_y^2}{(\varepsilon/R)^2} + \dfrac{x^2 + y^2}{R^2} - H_o)$	$E(r) = -\dfrac{mc^2}{qR}\dfrac{1}{R}(\dfrac{r}{R})[(\dfrac{\varepsilon}{R})^2 + 2\dfrac{I}{I_c}]$
Gaussian	$f = f_o \exp(-2\dfrac{p_x^2 + p_y^2}{(\varepsilon/R)^2} - 2\dfrac{x^2 + y^2}{R^2})$	$E(r) = -\dfrac{mc^2}{qR}\dfrac{r}{R}[\dfrac{\varepsilon^2}{R^2} + \dfrac{4I}{I_c}\dfrac{(1-\exp(-2r^2/R^2))}{2(r^2/R^2)}]$
Water bag	$f = f_o, \quad \dfrac{2}{3}(\dfrac{x^2+y^2}{R^2} + \dfrac{p_x^2 + p_y^2}{(\varepsilon/R)^2}) \leq 1$	$E(r) = -\dfrac{mc^2 r}{qR^2}[\dfrac{\varepsilon^2}{R^2} + \dfrac{8I}{3I_c}(1 - \dfrac{r^2}{3R^2})]$
Parabolic	$f = f_o(1 - \dfrac{x^2+y^2}{2R^2} - \dfrac{p_x^2 + p_y^2}{2(\varepsilon/R)^2})$	$E(r) = -\dfrac{mc^2 r}{qR^2}[\dfrac{\varepsilon^2}{R^2} + \dfrac{3I}{I_c}(1 - \dfrac{r^2}{2R^2} + \dfrac{r^4}{12R^4})]$
Extended Gaussian	$f = f_o \exp(-2\dfrac{p_x^2 + p_y^2}{(\varepsilon/R)^2} - \dfrac{(x^2+y^2)^2}{R^4})$	$E(r) = -\dfrac{mc^2}{qR}[(\dfrac{\varepsilon}{R})^2(\dfrac{r^3}{R^3}) + \dfrac{2I}{I_c}(\dfrac{R}{r})\,\mathrm{erf}(\dfrac{r^2}{R^2})]$

Table 8. Beam transmission efficiency and reduction of phase space density in RFQ due to errors in vane fabrication.

, microns	I = 0		I = 1 mA	
	$\dfrac{N_f}{N_o}$	$\dfrac{j_f}{j_o}$	$\dfrac{N_f}{N_o}$	$\dfrac{j_f}{j_o}$
1. 0	0.94	0.75	0.87	0.58
2. 50	0.92	0.73	0.85	0.56
3. 100	0.80	0.57	0.70	0.46
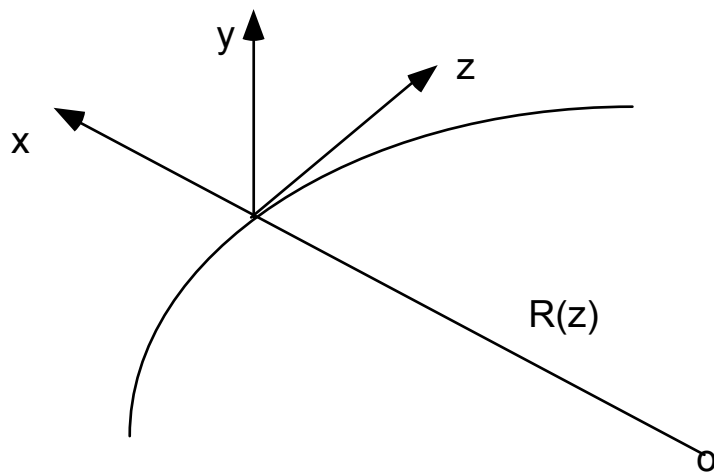
Fig. 1. Curvilinear system of coordinates.
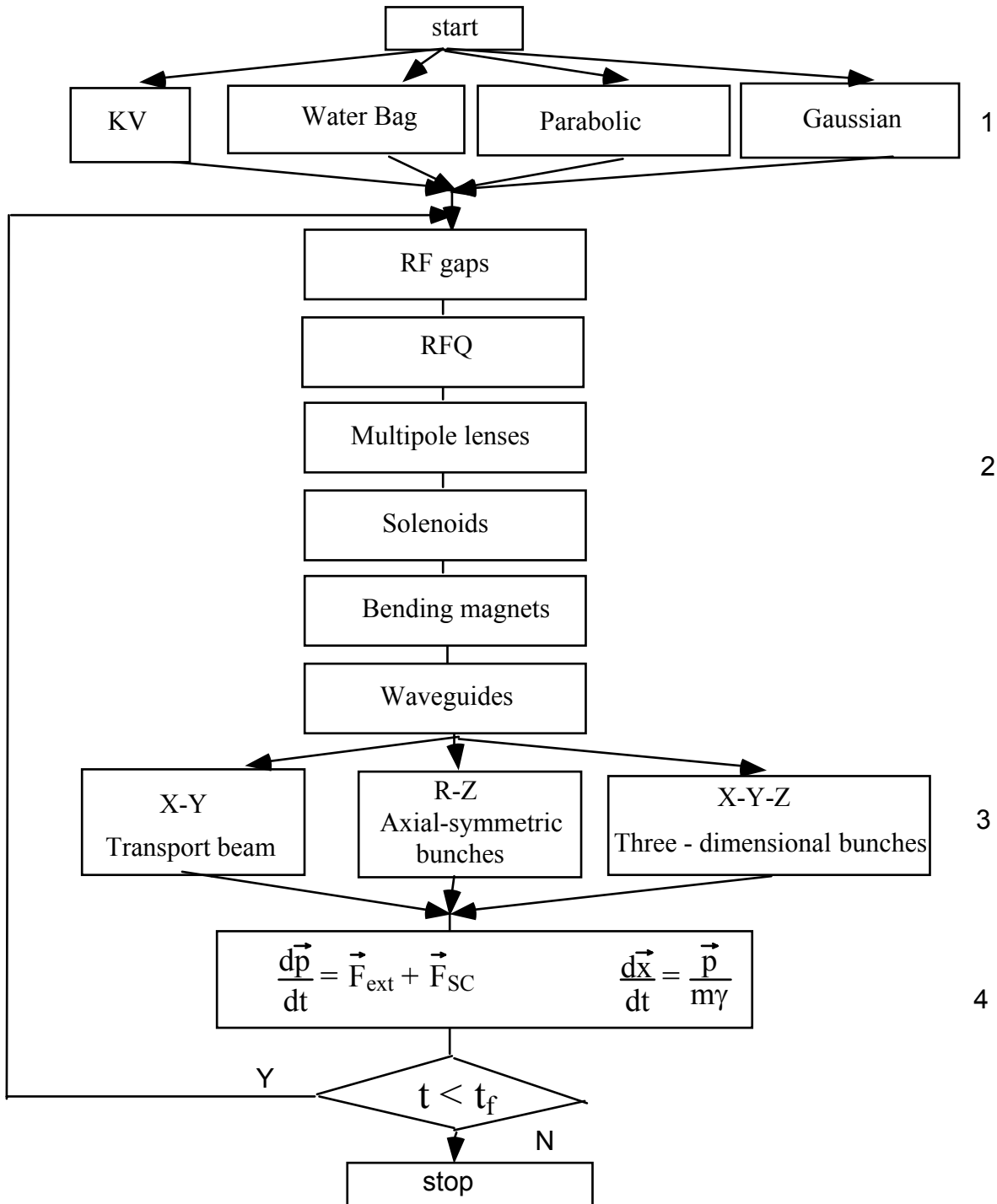
Fig. 2. Layout of code BEAMPATH for particle-in-cell beam dynamics simulation:

    1) generation of initial particle distribution in phase space

    2) calculation of external field

    3) calculation of space charge field

    4) integration of particle trajectories.
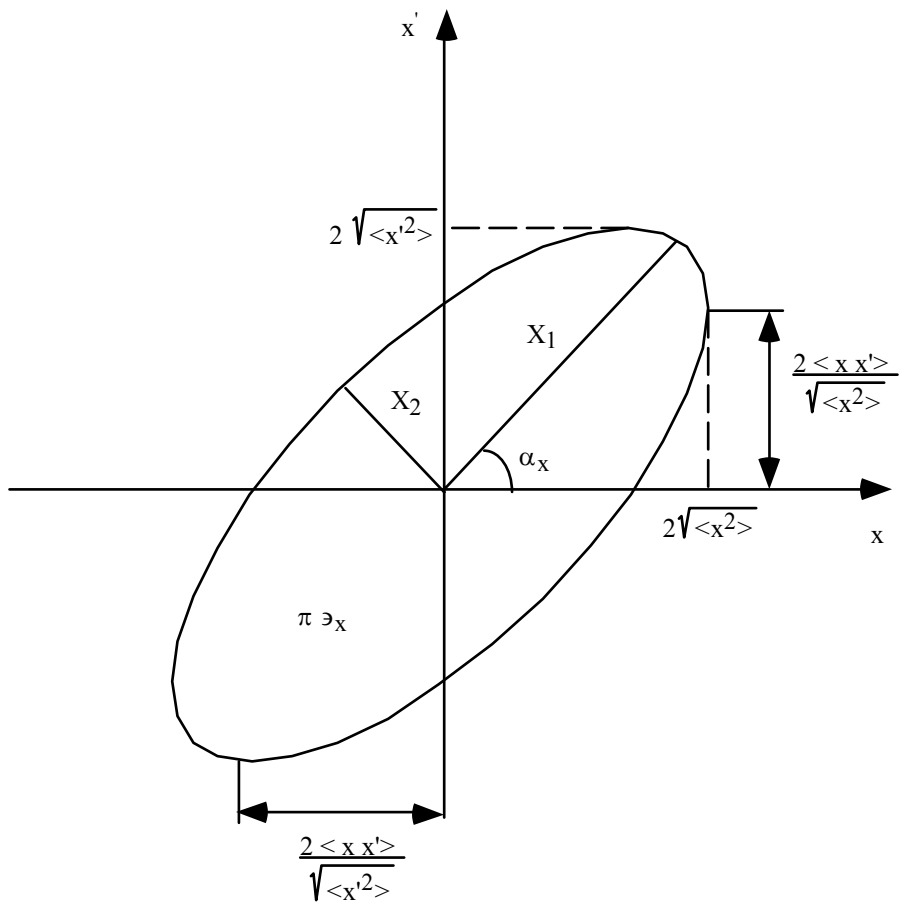
Fig. 3. Root-mean-square ellipse at phase plane (x, x').
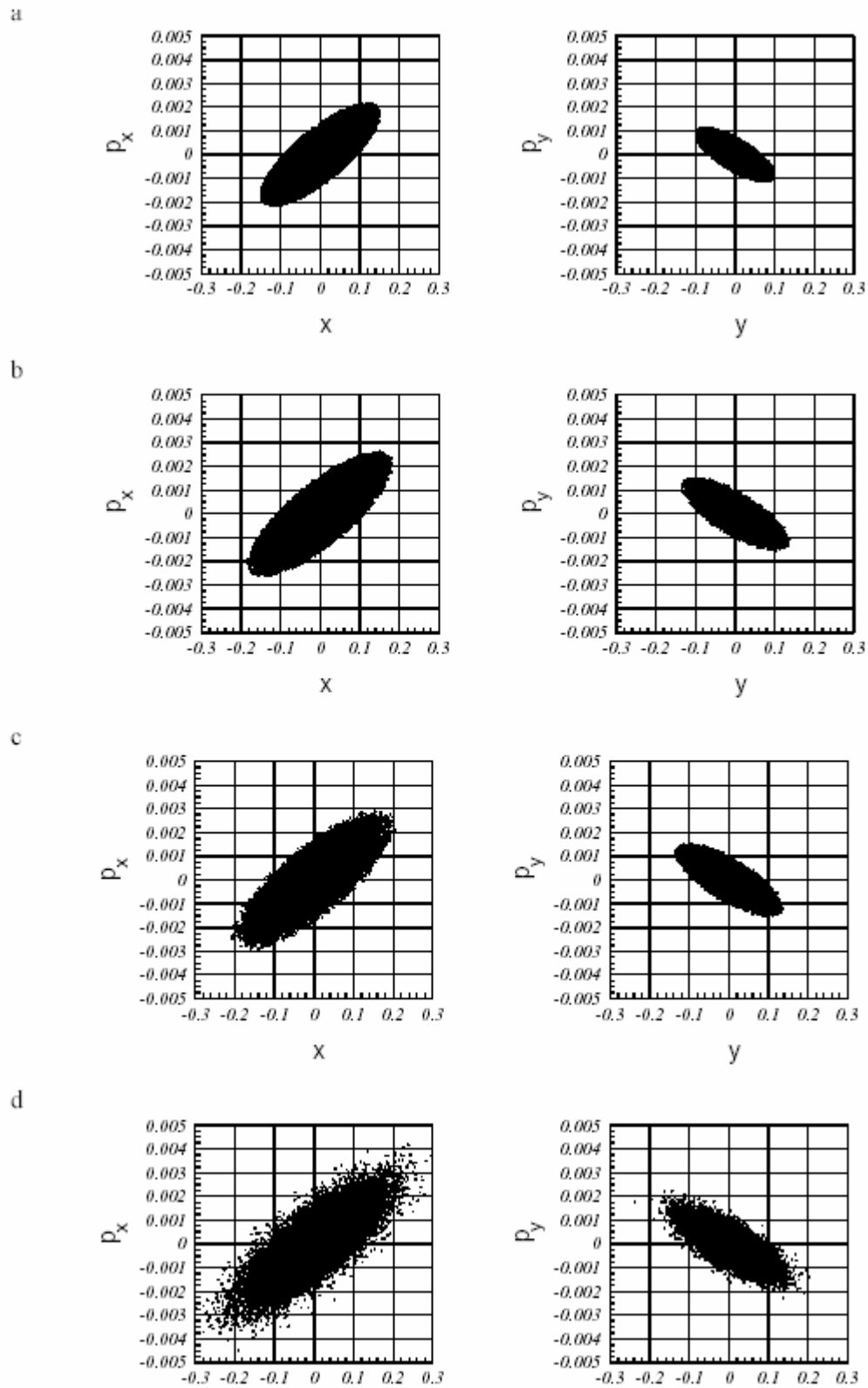
Fig. 4. Generation of particle distribution in phase space: ($\ni_x / \ni_y = 2.6$):
(a) KV, (b) "water bag", (c) parabolic, (d) Gaussian.
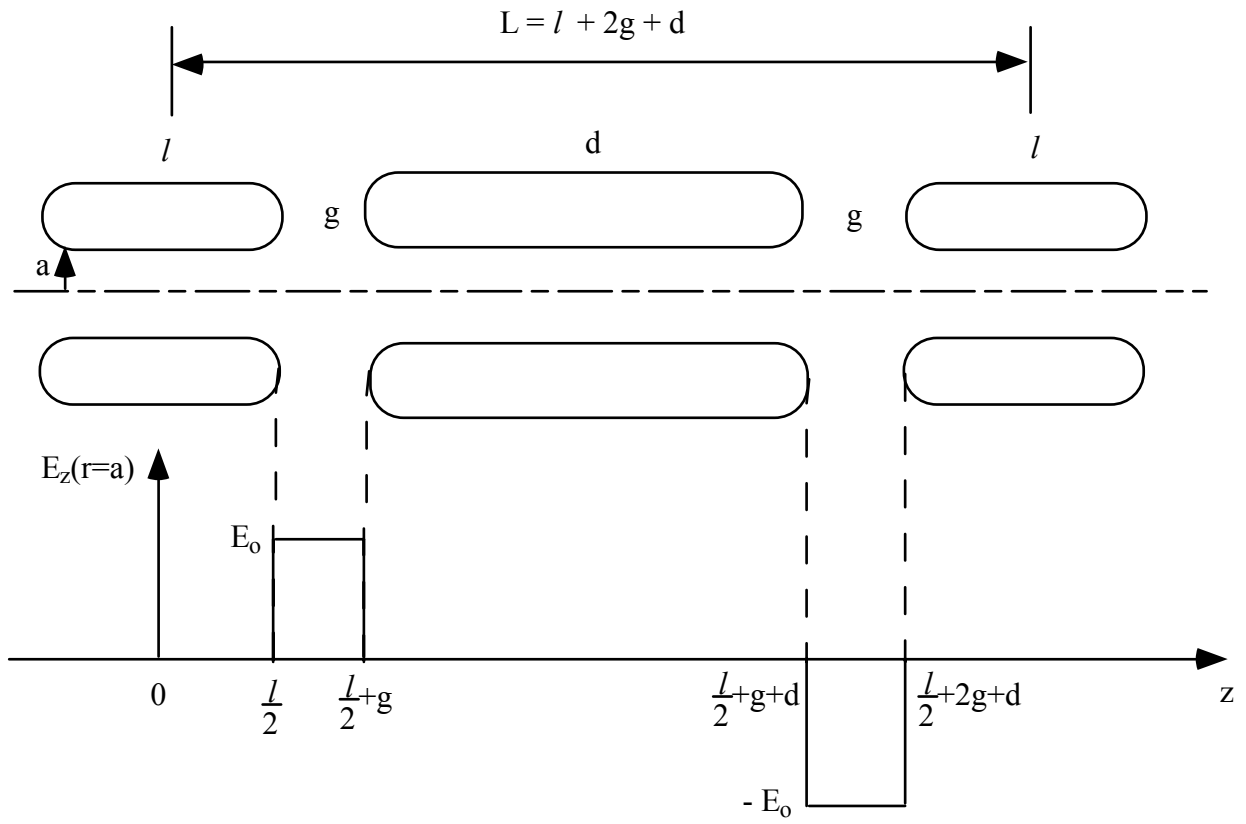
Fig. 5. Drift tube linac and approximation of field at the aperture boundary.
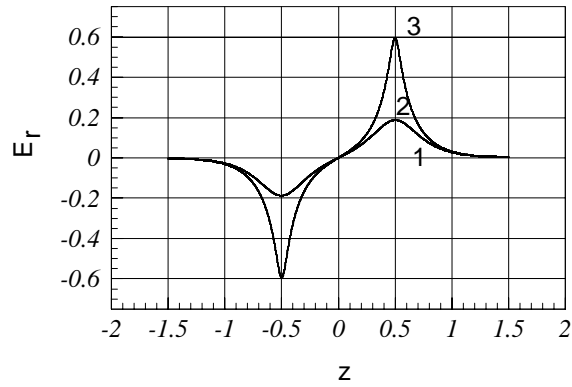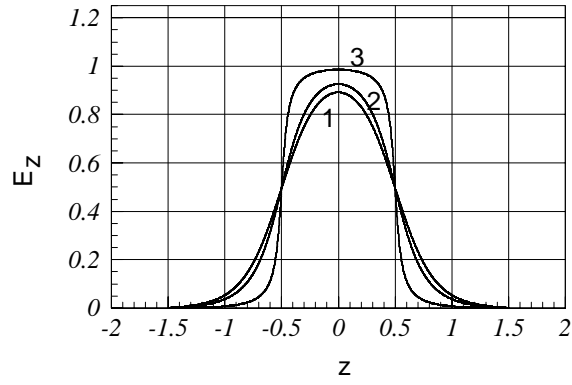
Fig. 6. Field distribution in RF gap: 1) $\frac{r}{a} = 0$, 2) $\frac{r}{a} = 0.5$, 3) $\frac{r}{a} = 0.9$.
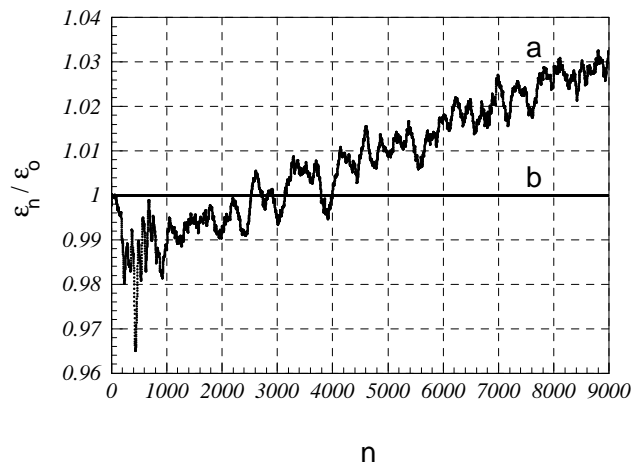
Fig. 7. Emittance growth of circular beam, $\tau = 1/300$: a) b = 17, $\delta E(R)/ E(R) = 0.01$, b) b = 0.

I = 0　　　　　　　　　　　　　I ≠ 0

n=0

n = 10^3
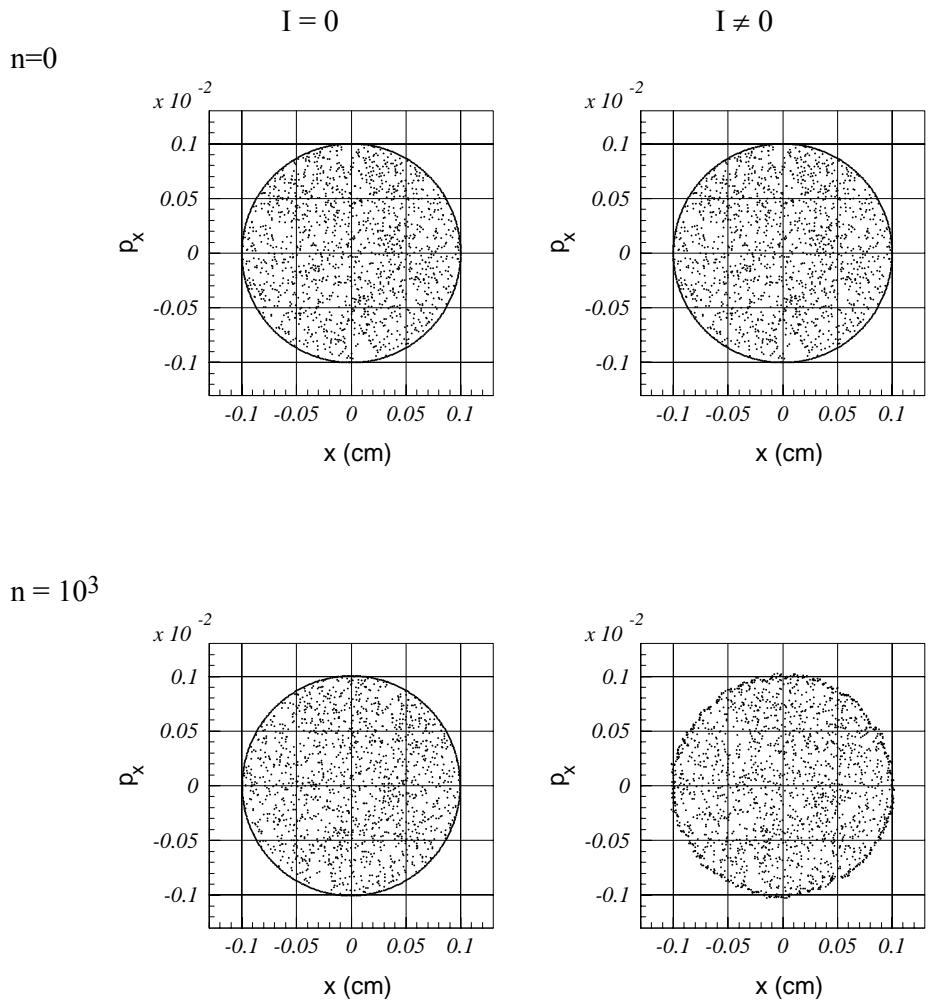
Fig. 8. Evolution of phase space area of the circular beam after 10^3 integration steps with and without space charge forces.
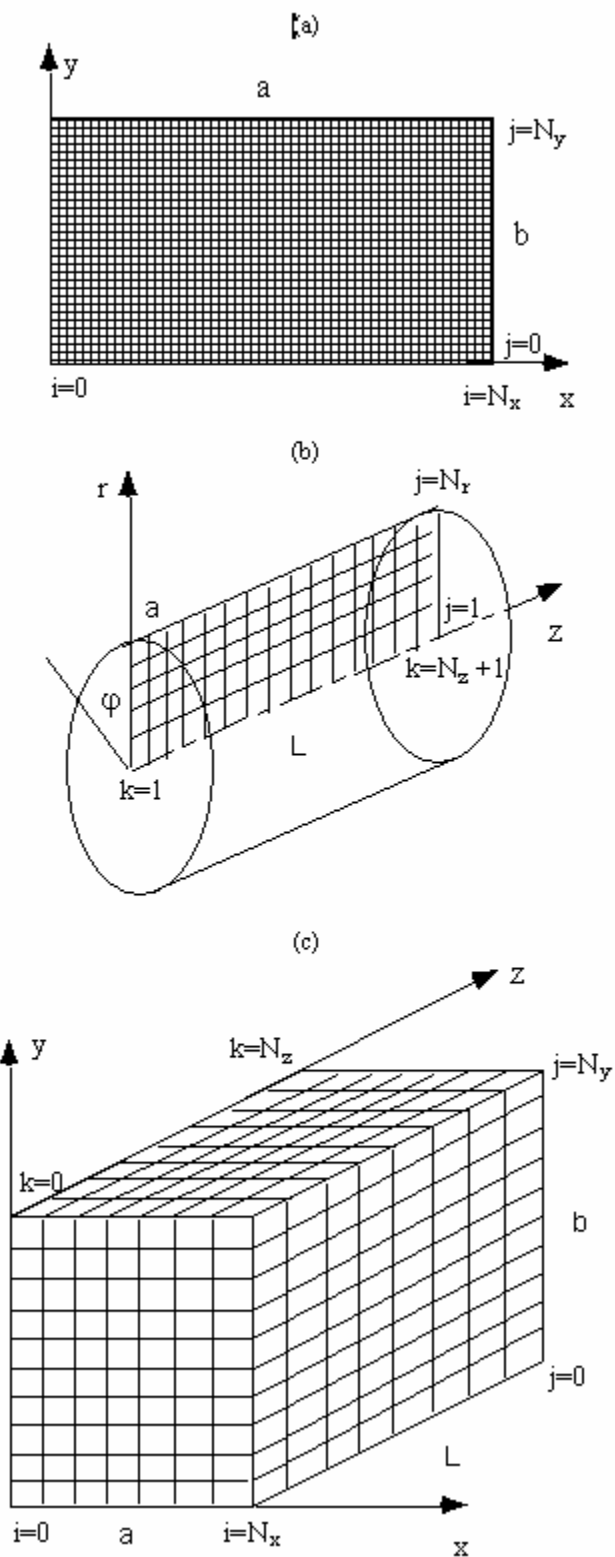
Fig. 9. Grid for solution of Poisson's equation: (a) z-uniform beam, (b) axial-symmetric beam, (c) beam with 3D particle distribution.
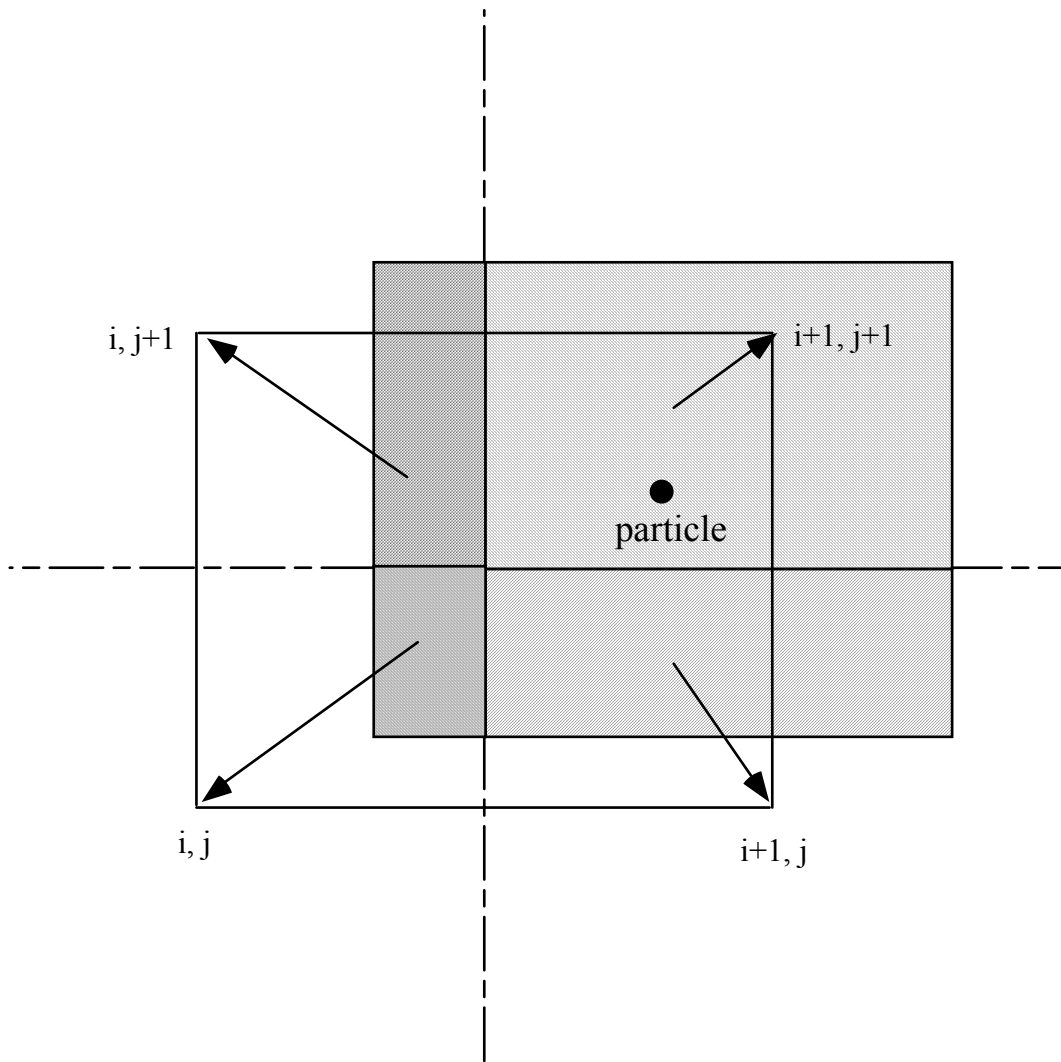
Fig. 10. Particle weighting on 2 dimensional grid: every node receives dashed fraction of particle charge.
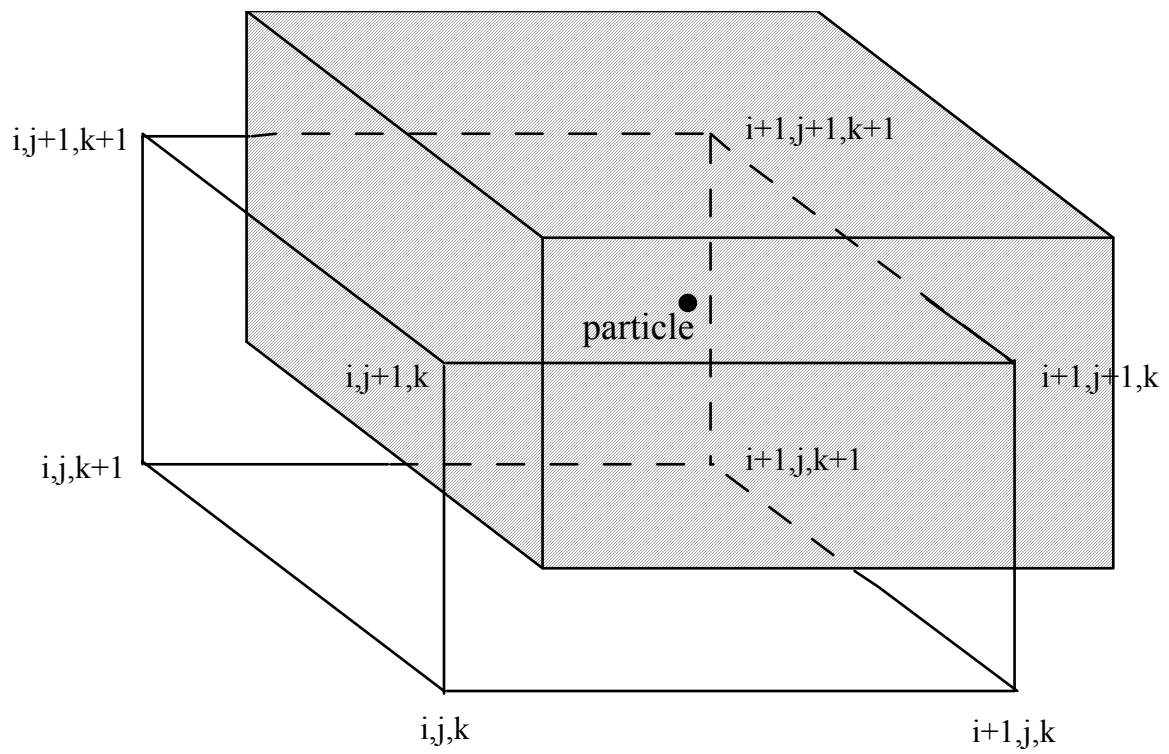
Fig. 11. Particle weighting on 3 dimensional grid.
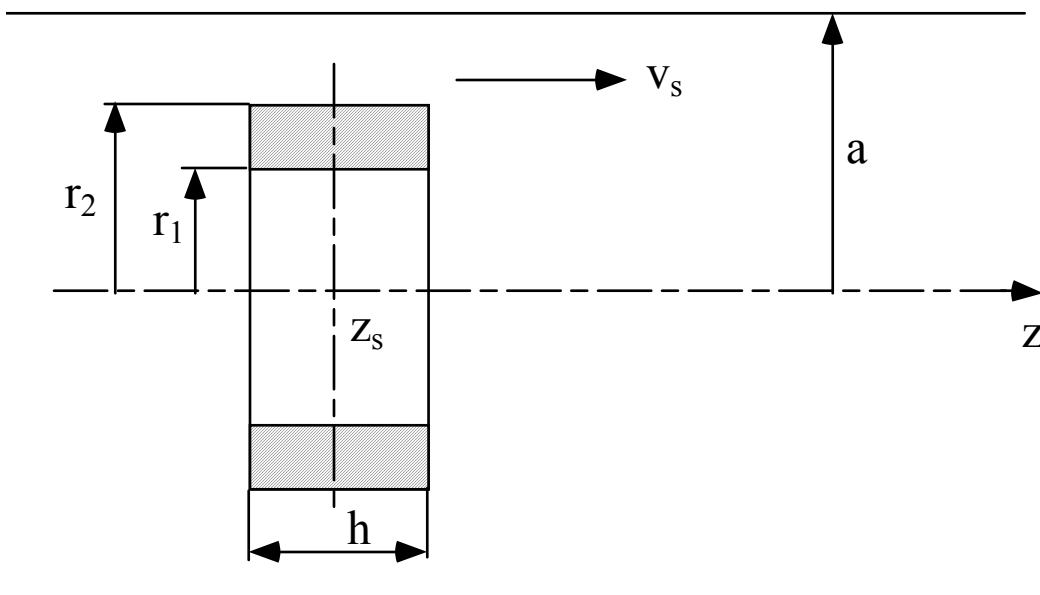
Fig. 12. On space charge calculation by Green function method.
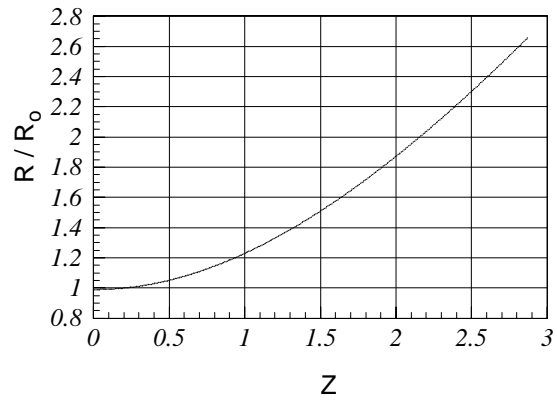
Fig. 13. Envelope of round uniform beam in free space.
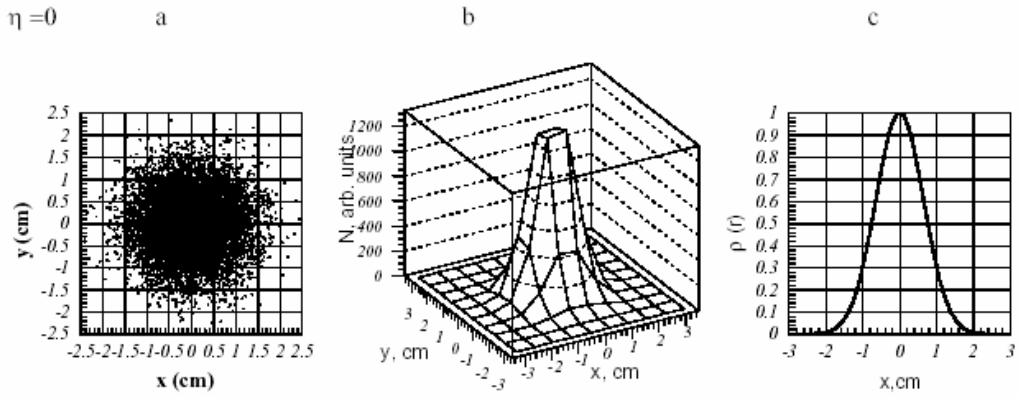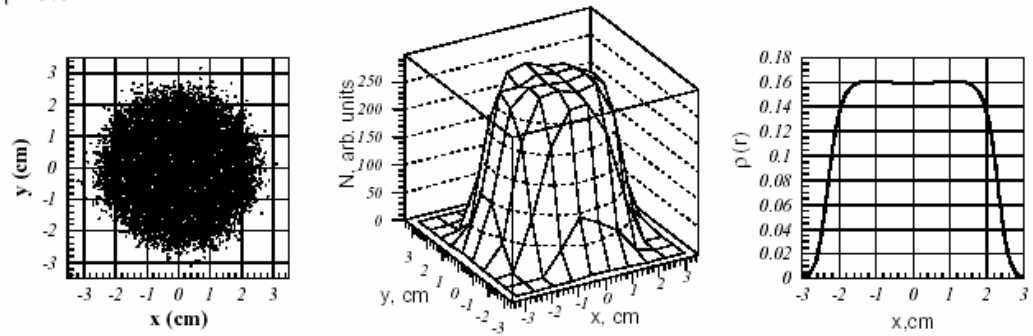
Fig. 14. Redistribution of Gaussian beam in drift space: a, b - PIC simulation, c - analytical solution, Eq. (8.3).

z = 0
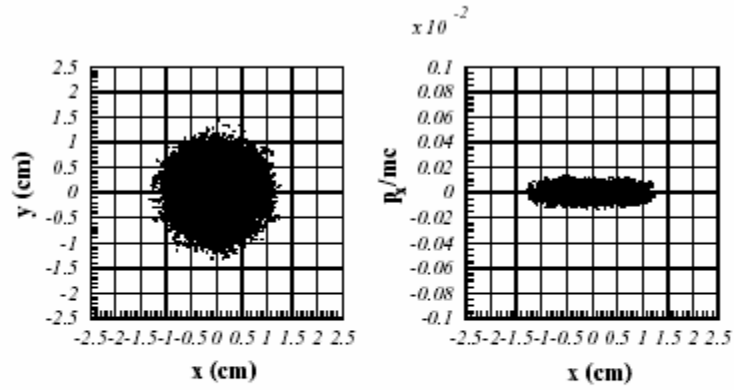
z = 15 cm
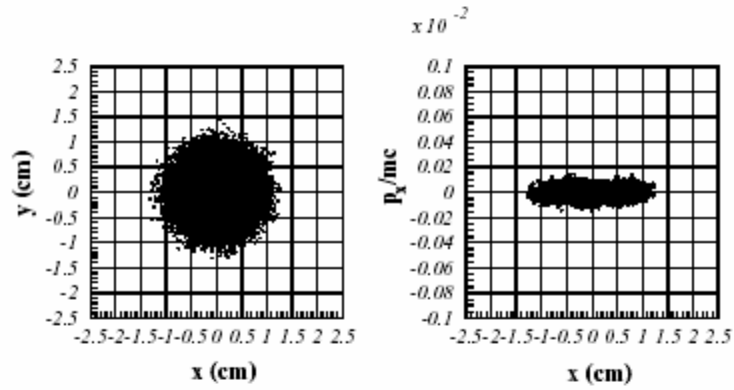
z = 80 cm
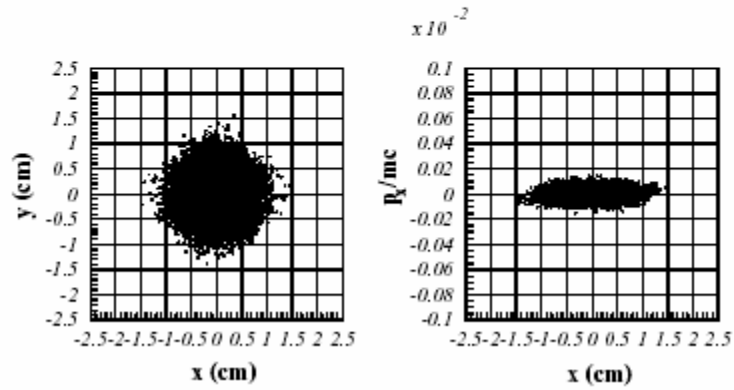
Fig. 15. Equilibrium of non-uniform beam in nonlinear focusing field.
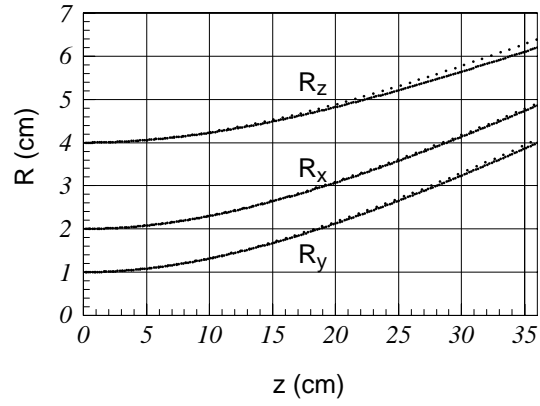
Fig. 16. Envelopes of uniformly populated ellipsoid in drift space: solid lines - PIC simulation, dotted lines - analytical solution of Eqs. (9.19) - (9.21).
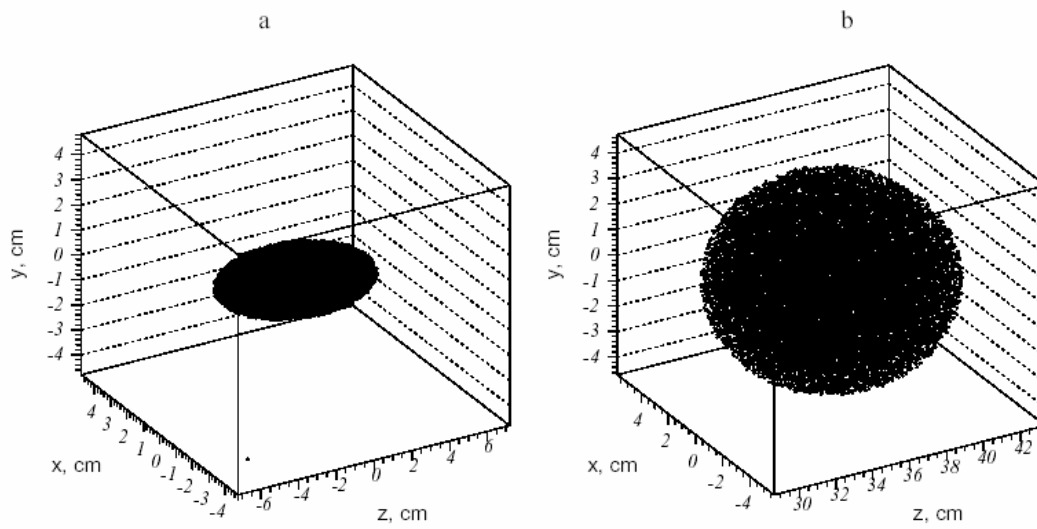
Fig. 17. Uniformly populated ellipsoid with charge of 3 nK and longitudinal velocity of $\beta_z = 0.01$ in drift space: (a) t = 0, (b) t = $1.2 \cdot 10^{-7}$ sec.
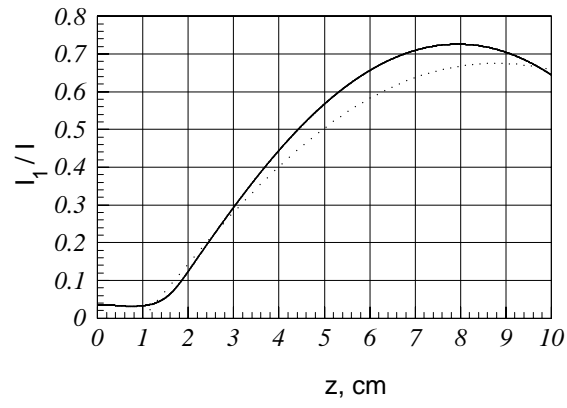
Fig. 18. Beam bunching: dotted line - analytical solution; solid line - numerical values.

a

b
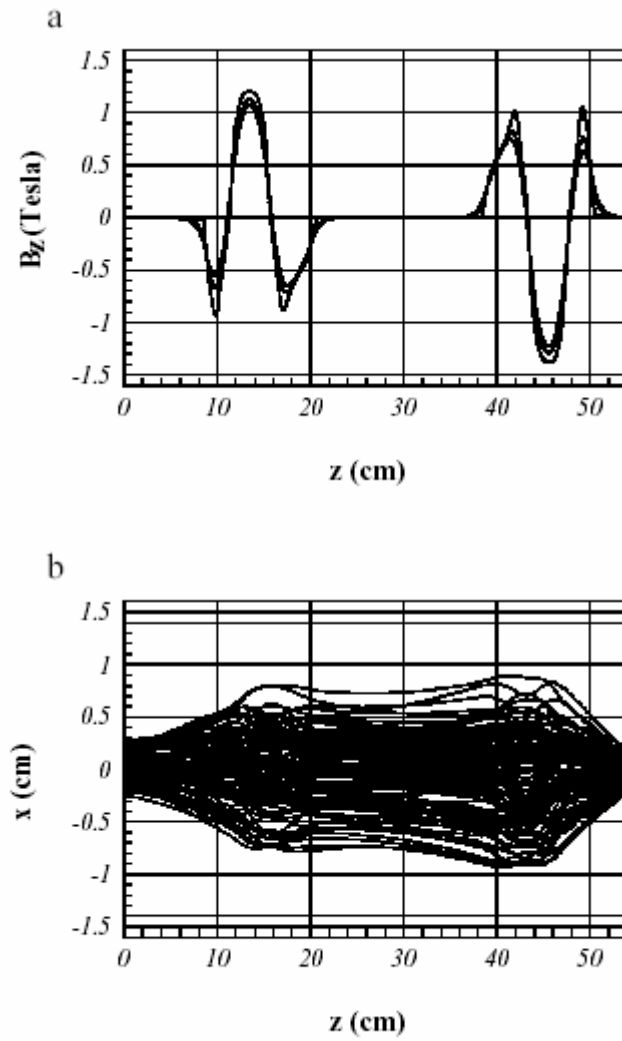
Fig. 19. (a) Magnetic field distribution and (b) particle trajectories of 50 keV, 20 mA, 0.075 π cm mrad proton beam.
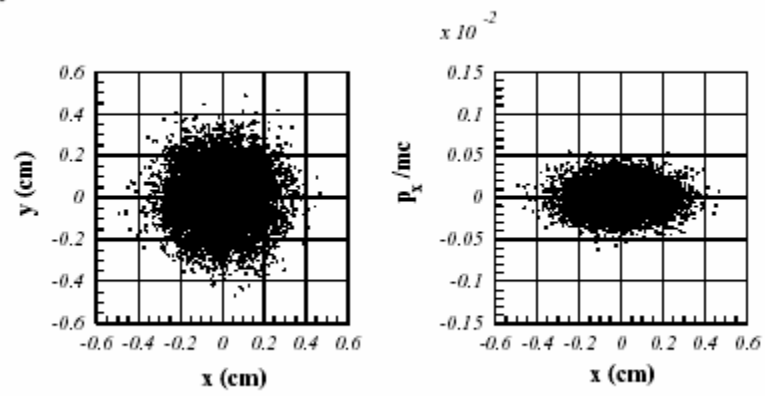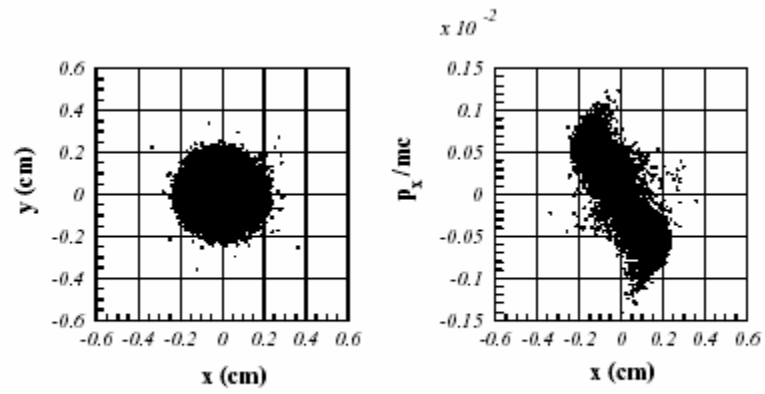
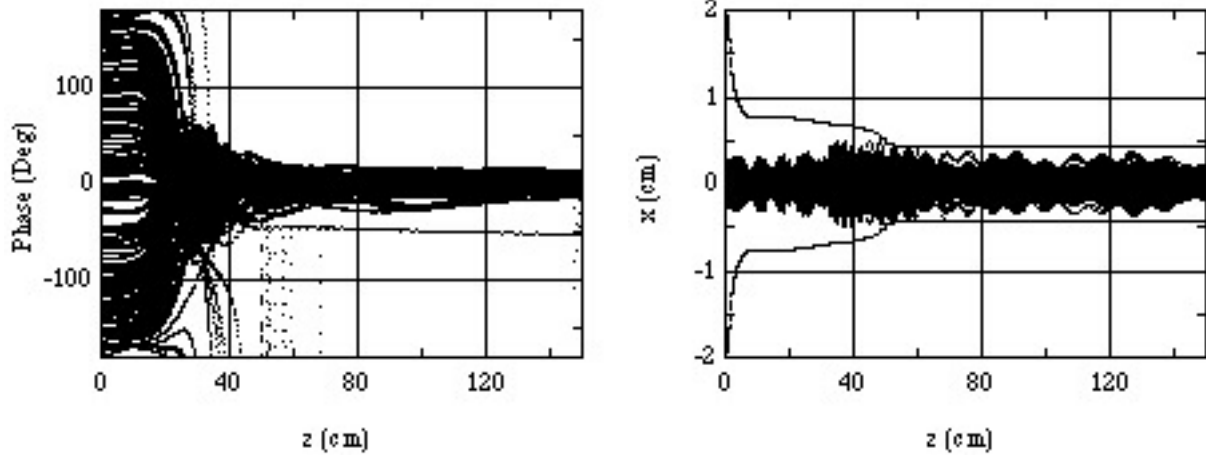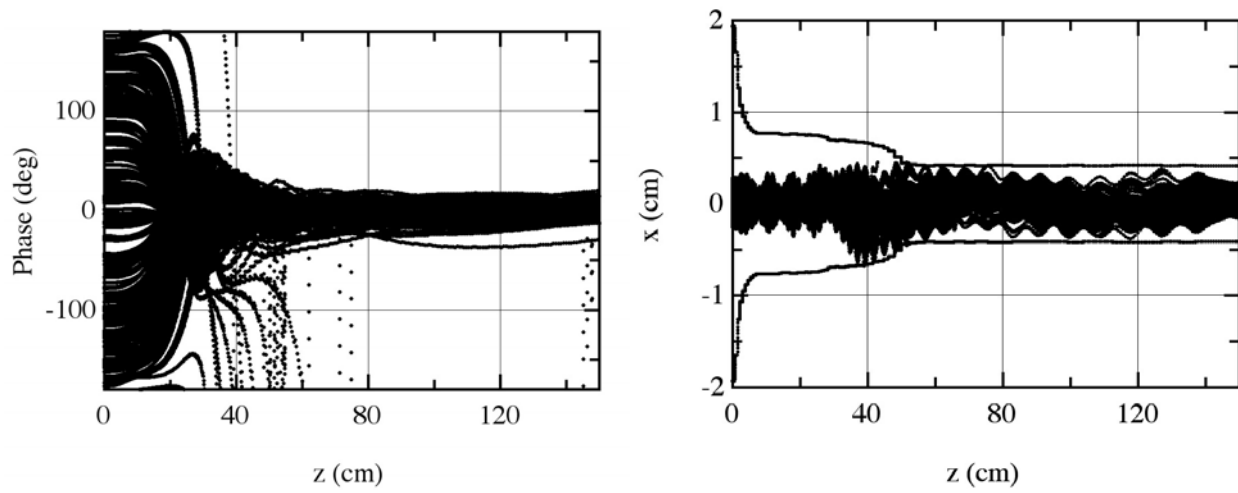Fig. 20. (a) Initial and (b) final particle distributions in LEBT.
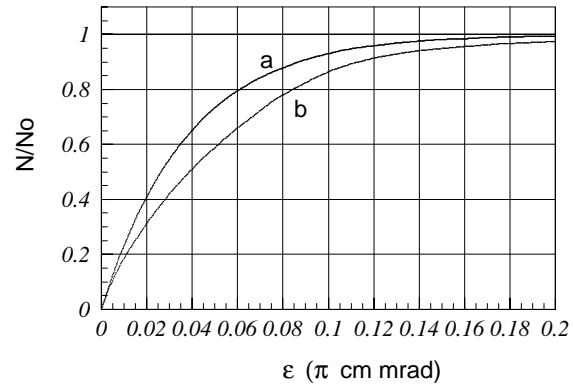
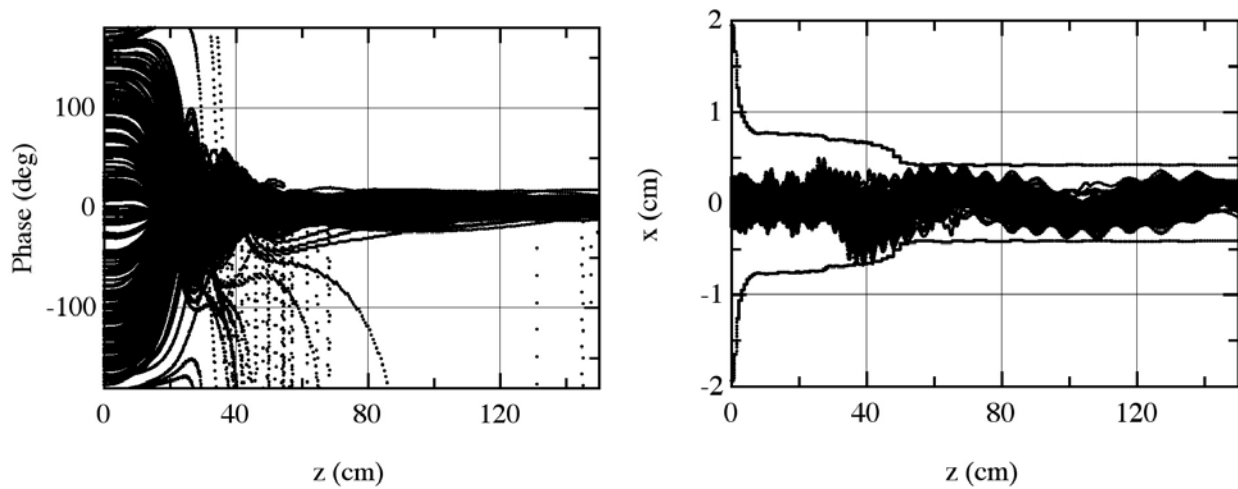Fig. 21. (a) Initial and (b) final beam phase space density distribution in LEBT.

a

b

c

Fig. 22. Phase space trajectories and x-trajectories in RFQ with different values of errors in vane tips fabrications: a) 0 microns, b) ± 50 microns, c) ± 100 microns.